Superconducting Spintronics in the Static and Dynamic Regime

Author :   D. van Dinter
Student ID :   1514229
Supervisor :   Prof.dr. J. Aarts
                                            Dr. K. Lahabi
                                          MSc. R. Fermin
2nd corrector :   Prof.dr.ir. S. J. van der Molen

Leiden, The Netherlands, January 10, 2021

Superconducting Spintronics in the Static and Dynamic Regime

D. van Dinter

Huygens-Kamerlingh Onnes Laboratory, Leiden University
P.O. Box 9500, 2300 RA Leiden, The Netherlands

January 10, 2021

Abstract

In this thesis S/F/S planair Josephson junctions in the static and dynamic regime are investigated. Clear SQUID interference patterns are observed in Co/Nb disks of different radii. In both cases, this indicates the splitting of the supercurrent channel. These channels are closely confined to the edges of the disk, making a compelling argument for the necessity of boundaries between superconductor, ferromagnet and vacuum for the generation of triplets with in-plane spin texture gradients. Furthermore, initial measurements on superconducting memory devices switched by spin texture alteration induced with in-plane fields show promises. Progress has also been made on the high frequency setup, enabling electronic measurements of devices while excitation with radio frequency Oersted fields takes place. Moreover, the results of micromagentic simulations support that significant spin texture alteration can be achieved with oscillating fields of proper frequency and amplitude. Here the focus is mainly on magnetic vortex gyration.

Cover picture: A visually edited example of a sample including the waveguide and the Co/Nb disks on the center stripline.

Contents

Introduction

Superconductivity has increasingly found its use in the world of technical applications in the form of, for instance, quantum computing and magnetic resonance imaging. These technologies rely on the substantial phase coherence and dissipationless transport properties of superconductivity. Furthermore, the feasible and beneficial union of superconducting platforms with the field of spintronics is emerging simultaneously. This untraditional marriage was long thought to be impossible to achieve, due to the inherent nature of the involved fermions. However, the confining boundaries set up by the Pauli exclusion principle are cleverly avoided by pairing the electrons in Cooper pairs not with opposite spin, but with opposite frequency or momentum components. This allows for the generation of equal-spin Cooper pairs that are unbothered by magnetic exchange fields: the spin triplets. The triplets can be further divided based on their pairing symmetry. The generation and static/dynamic alteration of the superconducting class of odd-frequency and even-momentum pairing forms the main subject of this thesis. This is motivated by the search for non-volatile memory devices and high frequency switching mechanisms in the fields of spintronics, superconductivity and neuromorphic computing.

Significant effort has been dedicated to the conversion of spin singlets to spin triplets. Strikingly, what is detrimental for ordinary singlets occurs to be essential for the generation of triplets: the presence of ferromagnetic order, or more accurately, a magnetic gradient. The configuration of the magnetic moments provides the means to control the superconducting transport properties. Thus far, multiple hybrid structures with different ferromagnetic layers are used to achieve this gradient in the form of magnetic non-collinearity (MNC), which effectively introduces the desired spin mixing and rotation (section 2.1). However, controlling the magnetization direction of individual magnetic layers is a difficult experimental feat to accomplish, let alone control. Recently, Lahabi et al. [1] have overcome this by utilizing the vortex spin texture of a single ferromagnetic disk. The in-plane exchange field gradient of the vortex spin texture of the disk is hypothesized to simultaneously enable spin mixing and rotation, leading to the generation of long range spin triplet supercurrents. The controllability of the magnetic vortex core, and therefore the spin texture, leads to a versatile platform in which the phase, amplitude and spatial distribution of the supercurrent can be altered [2]. At first, disks in the static regime with a larger radius than the conventional samples are investigated to get better insight in the spin triplet generation mechanism. But most prominently, as discussed in this thesis, two separate spin texture alteration mechanisms are explored. Introducing holes and therefore asymmetry in the disk geometry is discussed which opens up new avenues for non-volatile superconducting memory devices. Lastly, ferromagnetic resonance modes in magnetic disk structures induced by radio frequency (RF) fields generated in coplanar waveguides (CPW) are explored. These produce high speed spin texture alterations which are expected to have an effect on the supercurrent. Therefore, a new method is developed to utilize these RF field induced vortex modes to control spin triplet supercurrents. The cornerstone of the experiments are the micromagnetic simulations, which are utilized to determine suitable parameters for vortex pinning/depinning and resonance modes. They help both design the samples and explain the acquired experimental results.
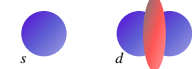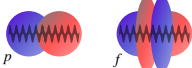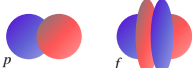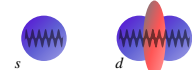
A theoretical background is given in the following chapter to better understand the underlying physical mechanisms at play in the device structure. The focus is mainly on magnetic vortex dynamics, since this is the most influential component governing the characteristics of the supercurrent in the dynamic regime. This is followed by an explanation of the basis of micromagnetic simulations. The third chapter elaborates on all the used methods in the fabrication process of the devices. Next, the results are displayed in an ordered fashion divided in simulation and experimental results. The conclusion is summarized in the last chapter, making arguments for the origin of spin triplet generation with planar spin texture gradient, the usability of this platform in superconducting memory devices and summarizing the progress made on dynamic devices.

Theory

2.1 Superconductivity and Triplet Generation

Superconductivity is the physical phenomenon that occurs in superconductors below a specific critical temperature T_C at which electrons pair up in a so-called Bose-Einstein condensate. The electrons form Cooper pairs, in which the Hilbert space drastically reduces in dimensionality, allowing for a macroscopic number of pairs to inhabit the same state. As a consequence, this allows for dissipationless transport of electrons, i.e. the resistance drops to *exactly* zero. The traditional way of looking at this mechanism is described in the BCS theory, in which Cooper pairs consist of electrons with opposite momentum and opposite spin. Electron-phonon interactions between the Cooper pairs and atomic lattice of the superconductor create an effective force on the Cooper pairs, overcoming the repulsive Coulomb force, allowing the electrons to travel without loss of energy. Furthermore, the entire macroscopic condensate can be described by a single wave function, generally termed the order parameter of the superconductor.

Noteworthy, the building blocks of Cooper pairs, the electrons, are fermions and therefore cannot inhabit the exact same quantum state. Another way of formulating this, is that their combined wave function has to be antisymmetric under particle interchange. This can be achieved by utilizing opposite spin components, which gives rise to the traditional singlet Coopers pairs as described in BCS theory. But this is not the only way to abide to the Pauli exclusion principle. The order parameter contains an additional frequency and momentum part which can correspond to an even or odd function. As long as the product of the three functions governing spin, frequency and momentum results in an odd function, the fermionic components can be combined into a bosonic Cooper pair. The type treated in this thesis is odd-frequency superconductivity, in which the electrons form triplet pairs of equal spin. Figure 2.1 shows a table with the plausible pairing symmetries for Cooper pairs.

Spin	Frequency	Momentum		
Singlet (Odd) ↑↓ - ↓↑	Even	Even	s	d
	Odd	Odd	p	f
Triplet (Even) ↑↑ ↓↓ ↑↓ + ↓↑	Even	Odd	p	f
	Odd	Even	s	d

Figure 2.1: *Table showing the plausible pairing symmetries for Cooper pairs, inspired by Lahabi et al. [1]. The main subject of this thesis is shown in green, triplet Cooper pairs of odd-frequency and even-momentum pairing.*

Triplet superconductivity does not suffer from the same drawbacks that singlet Cooper pairs experience under the exchange field of a ferromagnet. For singlets the magnetic interaction energy forces the spin of both electrons in the same direction, effectively breaking the Cooper pair and losing all the interesting physics that accompanies the condensate. On the contrary, triplets can survive for a relative long range in ferromagnets, unbothered by the enforced ferromagnetic order of the exchange field. The occurrence of triplet superconductivity is unfortunately a rarity in nature, while it certainly holds technological promises. For this reason many groups have invested theoretical and experimental efforts into the generation of spin triplet supercurrents, generally utilizing the proximity effect in multi-stack ferromagnetic architectures [3–6]. The proximity effect describes the leakage of the order parameter into an adjacent medium. This has as a consequence that supercurrents can flow for a certain distance in non-superconductors. The coherence length ξ in the proximized material is the characteristic length scale over which the order parameter falls off and therefore defines the survivability of the supercurrent outside of the superconductor. It is material specific, since certain materials are more tolerant to the presence of the condensate than others. This behaviour has led to the extensive field of Josephson junction mechanics, in which multi-layered junctions are constructed to specifically exhaust the proximity effect as displayed in Figure 2.2a. Commonly, a weak link (be it an insulator, ferromagnet or normal metal) is placed between two superconductors. The order parameter of the two superconductors leaks into the weak link and, as discovered by Brian David Josephson [7], the phase difference between the order parameters of the superconductors on opposite sides drives a supercurrent through the weak link.

a

b
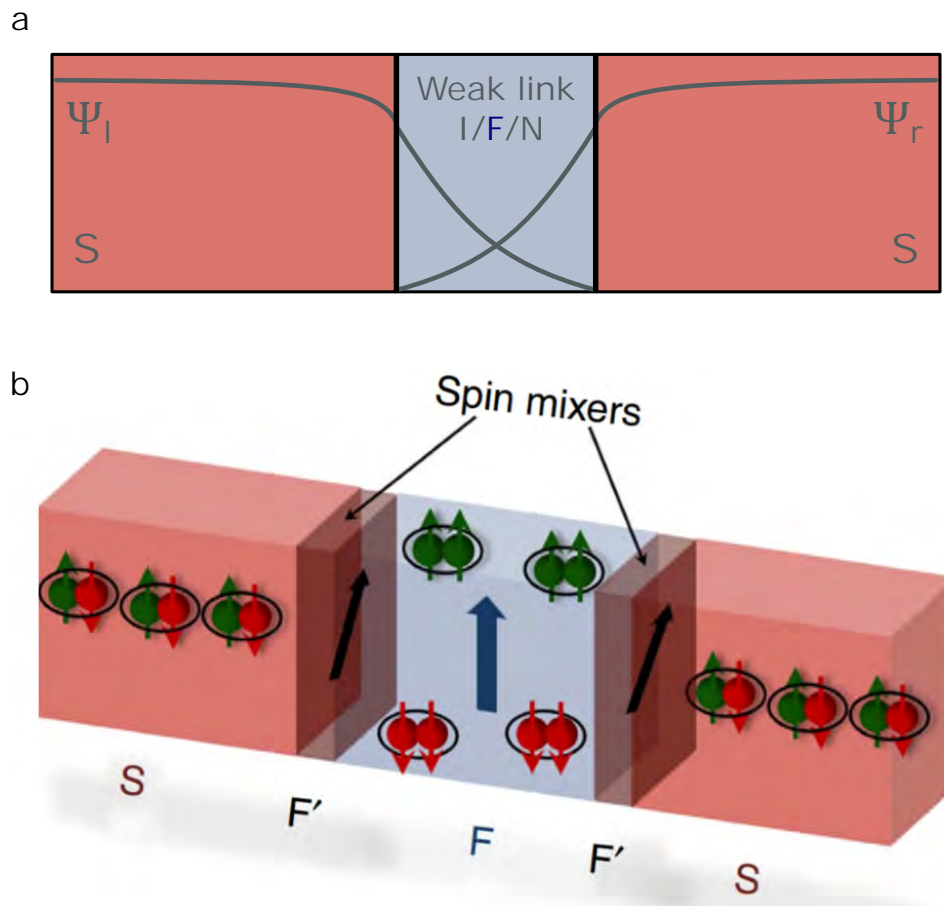
Figure 2.2: *(a) A schematic overview of the proximity effect in a Josephson junction structure. (b) A multi-layered ferromagnetic Josephson junction indicating the separate spin mixing (F') and rotation (F) layers adapted from Banerjee et al. [5].*

The idea was to use this type of junction in combination with a ferromagnetic weak link. An individual ferromagnet would mix the spin components of the arriving spin singlet correlations, in a process fittingly named spin mixing. These spin triplets are rather short-lived since they are not spin-polarized, and for this reason the additional process of spin rotation was introduced in an extra ferromagnetic layer. The ferromagnet responsible for the spin rotation has a different magnetization direction than

the original spin mixing layer, giving rise to the non-collinear magnetic profile along the junction and effectively rotating the spin-quantization axis. As a result, the spin projection of the triplets aligns with the exchange field of the spin rotation layer. This spin polarizes the supercurrent and thereby creates the long-ranged spin triplet correlations. This type of Josephson junction with a multi-layered magnetic non-collinear weak link can be seen in Figure 2.2b.

Our group has achieved spin triplet generation in which the spin mixing and rotation procedures are expected to take place in one single Cobalt ferromagnetic disk. The occurrence of a stable vortex ground state splits the supercurrent in two paths. The supercurrent density is mostly confined along the edges of the disk. This is partly attributed to be the effect of the extremely high magnetic direction gradient of the vortex core, effectively turning the device in the equivalent of a superconducting quantum interference device (SQUID). However, the degree of confinement of the edge channels is still unexplained. It has come to light that the presence of a vortex spin texture introduces many possibilities regarding the control of the supercurrent in terms of amplitude, phase and spatial distribution. Hence, a significant part of the following theoretical background will be dedicated to vortex dynamics, in order to better understand vortex movement/displacement under static magnetic fields (the static regime), spin-polarized currents and RF fields (the dynamic regime).

2.2 Magnetic Spin Texture Dynamics

This section examines the magnetic dynamics influencing the spin texture in the device. An overview will be given of the relevant physical concepts which aids the interpretation of the experimental results. Focus is placed on the magnetic vortex, since this entity has far reaching consequences for the operation mechanisms in the superconducting disk and plays a central role in the memory application.

2.2.1 The magnetic energy landscape

As is generally the case in physics, systems favor finding the minimum in their energy landscape and thereby reaching a stable ground state. This is no different for spin textures in nano-patterned devices. In ferromagnetic systems, the total energy is defined by:

$$E_{total} = \int_V (\epsilon_{exchange} + \epsilon_{demagnetization} + \epsilon_{anisotropy} + \epsilon_{external}) dV \tag{2.1}$$

The first term describes the exchange energy the individual spins feel as a result of the effective exchange field originating from the spins in their vicinity, ranging a distance of the magnetic exchange length (generally in the order of $1 - 10$ nm). This is the characteristic length scale over which spins feel the interactions with their neighbours and is given by:

$$l_{exchange} = \sqrt{\frac{2A}{\mu_0 M_s^2}} \tag{2.2}$$

In which A denotes the exchange stiffness in units of J/m and is a measure for the exchange strength between spins in a certain ferromagnetic material. M_s is the saturation magnetization in units of Tesla (T), signifying the upper bound of the magnetic field above which the material is not magnetized any further. It must be noted that the in-plane (IP) or out-of-plane (OOP) values for M_s can differ for certain materials. For a ferromagnet the spins prefer to point in the same direction, lowering the total Hamiltonian of the system. The second term in equation 2.1 describes the effect of the demagnetizing field, commonly referred to as the stray field. It reflects the tendency of the field to reduce the total magnetization of the system. The demagnetization component causes the spin to align parallel to the surface of the ferromagnet, minimizing magnetic surface charges and therefore lowering the stray fields. Furthermore, the anisotropy energy accounts for the presence of a magnetic easy-axis, in which certain crystallographic directions are energetically more favourable to magnetize along than others. While these three terms are intrinsic properties of the ferromagnet, the external (Zeeman) energy can be controlled experimentally by tuning the external magnetic field. Spins prefer to align themselves with this field in order to lower the external energy contribution. The fields arising from these interactions are generally combined into one total effective field H_{eff}.

2.2.2   The Landau-Lifshitz-Gilbert equation

When considering the dynamics of spin textures under different types of interactions, it is common to replace the discrete spin distribution by a continuous magnetization function of space and time $M(r,t)$. This is normalized with respect to the saturation magnetization M_s, given the unit magnetization vector $\mathbf{m} = \mathbf{M}/M_s$. The dynamic response of the system under application of external field is described by the Landau-Lifshitz-Gilbert (LLG) equation:

$$\frac{\partial \mathbf{m}}{\partial t} = -\gamma \mathbf{m} \times \mathbf{H}_{eff} + \alpha \mathbf{m} \times \frac{\partial \mathbf{m}}{\partial t} \tag{2.3}$$

Where γ is the gyromagnetic ratio and α denotes the Gilbert damping parameter. The first term describes the precession of the spin around the axis of H_{eff}, while the second term forces the precessing spins to align with the H_{eff} through damping. It is important to realize however, that the spin texture can also be significantly altered by spin-transfer torque processes and RF field contributions, which must be included accordingly to the right-hand side of equation 2.3. The three main states described by the LLG equation are shown in Figure 2.3: the equilibrium, excitation and dynamic motion state.
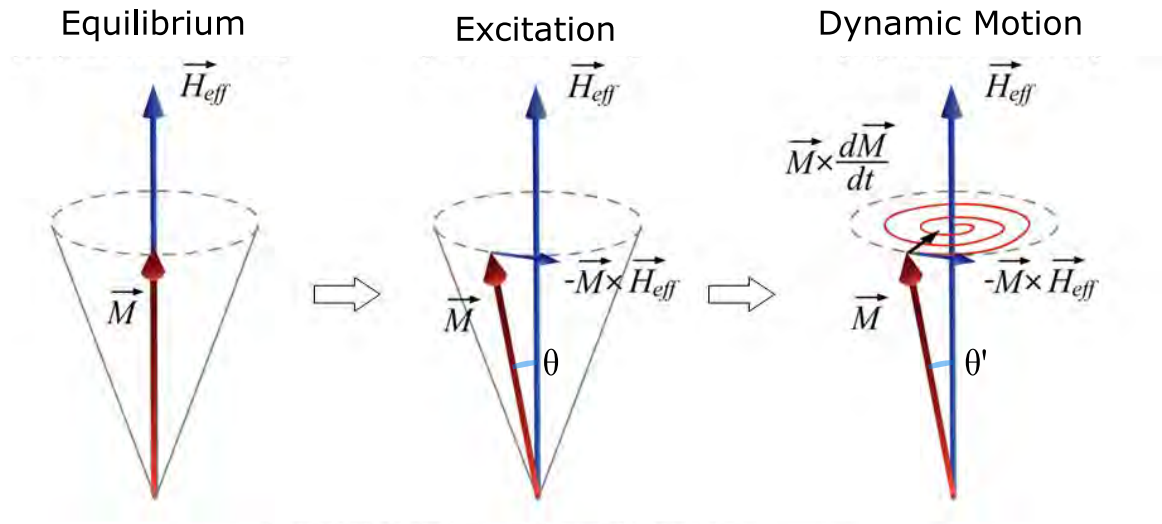

Figure 2.3: *The three states of the LLG equation showing the equilibrium, excitation and dynamic motion state [8].*

The LLG equation serves as a powerful tool to describe spin texture dynamics of ferromagnetic systems and depending on the geometry of the sample, one of the stable state solutions can contain a magnetic vortex. This vortex configuration consists out of a curling IP spin texture with an OOP component at the core. Specifically the interplay between the exchange and magnetostatic interactions are responsible for its formation. The demagnetization interaction causes the spins to follow the boundary of the disk, giving rise to the curling spin texture. Moreover, when approaching the centre, the exchange interaction dominates over the demagnetization interaction and forces the spins in the centre of the disk to point OOP, leading to the formation of the vortex core. Inherent to the geometry of our system, this spin texture is a stable ground state in which the total energy is minimized. The occurrence of an OOP component at the vortex core should not come as a surprise, since the exchange energy would drastically increase if the spins would remain IP, resulting in an energetically unfavourable configuration. The two main fundamental properties of the vortex configuration are its polarity p and chirality c. The polarity denotes the direction of magnetization of the vortex core with $+1$ for the up-state and -1 for the down-state. The chiralty describes the sense of rotation with $+1$ for clockwise (CW) curling and -1 for counterclockwise (CCW) curling. The product of polarity and chiralty gives the handedness of the vortex state. Mirror symmetry reduces the number of possible states from four to two: $+1$ for right-handed (RH) and -1 for left-handed (LH) configurations. A couple of spin textures with and without a vortex state are presented in Figure 2.4a.
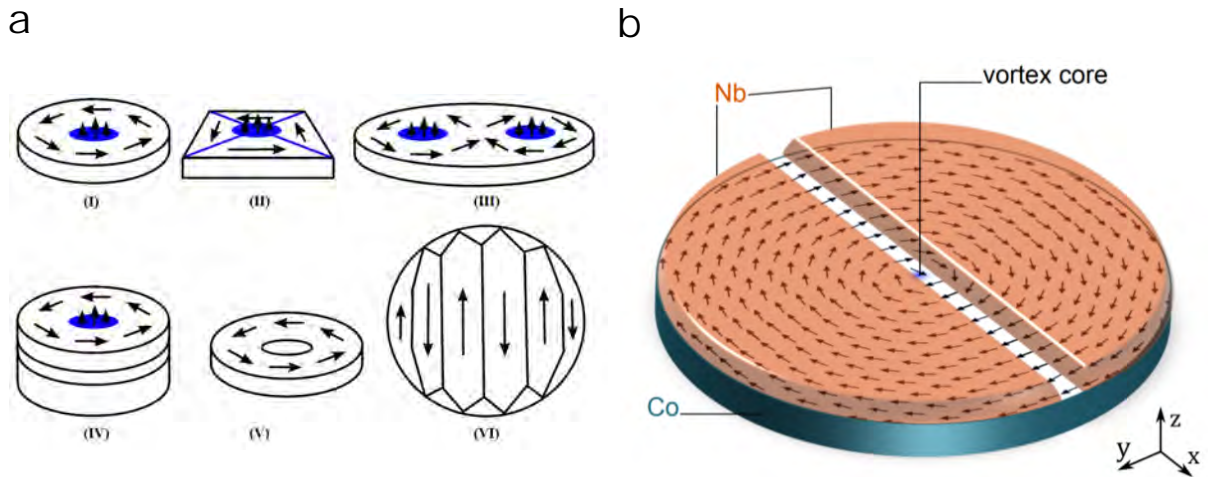
Figure 2.4: *(a) Six different magnetic structures with a vortex state (I, II, III and IV) and without a vortex state (V and VI) as seen in Antos et al. [9]. (b) The magnetic Co disk with superconducting Nb contacts under consideration [1].*

For suitable dimensions, configuration I, II , III and IV can contain a stable vortex state. Configuration I shows a circular disk with a magnetic vortex at the center and represents the investigated sample (as shown in Figure 2.4b) most accurately. For elliptical disks (III), the ground state can contain two vortices of opposite handedness, located at the focal points. Furthermore, changes in geometry (V) or multidomain structures with dominating magnetic anisotropy (VI) can get completely rid of the magnetic vortex state. Nevertheless, the magnetic dynamics of configurations that do harbor a magnetic vortex are greatly affected by its presence. This raises the question which cylinder dimensions suffice for a stable vortex state and this is treated in the simulation section of the results. When treating the simple case of static field sweeps, the behaviour of the vortex can be understood quite intuitively when considering Figure 2.5.
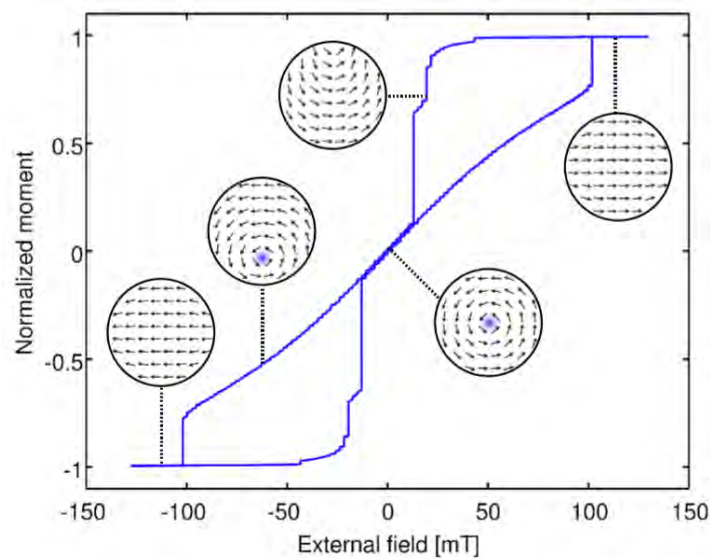
Figure 2.5: *Magnetic hysteris loop (blue line) and configuration snapshots representing the movement of the vortex in a cylindrical Permalloy disk while experiencing an IP field along the x-axis adapted from Antos et al. [9].*

Applying an external magnetic field enlarges the subsection of the spin texture which lies parallel to this field. This results in a vortex movement perpendicular to the external field, away from the enlarging section. This process continues until the vortex is pushed out of the system, where the vortex annihilates at the annihilation field. As the field is lowered to zero, an intermittent C-shaped phase is observed in the spin texture before the vortex re-enters. The field strength at which re-entrance occurs is coined the nucleation field. However, a more rigorous and analytical framework is needed to explain the vortex dynamics in the dynamic regime, in which alternating currents and radio frequency fields are present.

This can be achieved by simplifying the system by treating the vortex as a quasi-particle in which the motion of the vortex center ($\mathbf{X} = [X_1, X_2]$) is governed by the equation of motion derived from the Lagrangian formalism. This Lagrangian was derived by Shibata et al. [10] and includes the effect of spin-transfer torque processes on the energy landscape. It is given by:

$$\mathcal{L}_V = \frac{1}{2}\mathbf{G} \cdot (\dot{\mathbf{X}} \times \mathbf{X}) - U(\mathbf{X}) - \mathbf{G} \cdot (\mathbf{v}_s \times \mathbf{X}) \tag{2.4}$$

Where $\mathbf{G} = (\hbar S/a^3)2\pi L p q \hat{\mathbf{z}}$ is the gyrovector with $\hbar$ the reduced Planck constant, S the spin magnitude, a the lattice constant, L the thickness of the disk, p the polarization and q the vorticity, respectively. $U(\mathbf{X})$ represents the potential energy contribution coming from magnetostatic interactions and the last term describes the current-induced spin-transfer torque. Using the Euler-Lagrange for X, the equation of motion of the vortex core can be derived. However, one has to add the so-called dissipation function $W = \alpha D \dot{\mathbf{X}}^2/2$, to properly take into account the effect of Gilbert damping. Here α denotes the Gilbert damping constant and D a dissipative constant. This results in the modified Euler Lagrange equation and the corresponding equation of motion for the vortex core [10]:

$$\frac{d}{dt}\frac{\partial \mathcal{L}_V}{\partial \dot{\mathbf{X}}} - \frac{\partial \mathcal{L}_V}{\partial \mathbf{X}} = -\frac{\partial W}{\partial \dot{\mathbf{X}}} \rightarrow \mathbf{G} \times (\mathbf{v}_s - \dot{\mathbf{X}}) = -\frac{\partial U(\mathbf{X})}{\partial \mathbf{X}} - \alpha D \dot{\mathbf{X}} \tag{2.5}$$

This equation is named the Thiele equation and can be used to describe the effect of current-induced spin-transfer torque on the displacement of the vortex core. When treating a fully spin-polarized DC current and harmonic potential, the vortex moves in a spiral trajectory in which the resulting end-displacement is directly proportional to the current density. The rotational direction (clockwise or counter-clockwise) of the trajectory depends on the sign of the core polarization [10]. When displacing the vortex core from its equilibrium position, the vortex moves in a circular trajectory until it finds its ground state again at the center of the disk (Figure 2.6a) as simulated by Wysin et al. [11]. While the vortex continues its movement, the positional oscillation in the x-direction is out of phase with respect to the oscillation of the IP magnetization in the y-direction (Figure 2.6b). These simulations agree to a high degree of accuracy with the results of the Thiele equation [11].

a

b
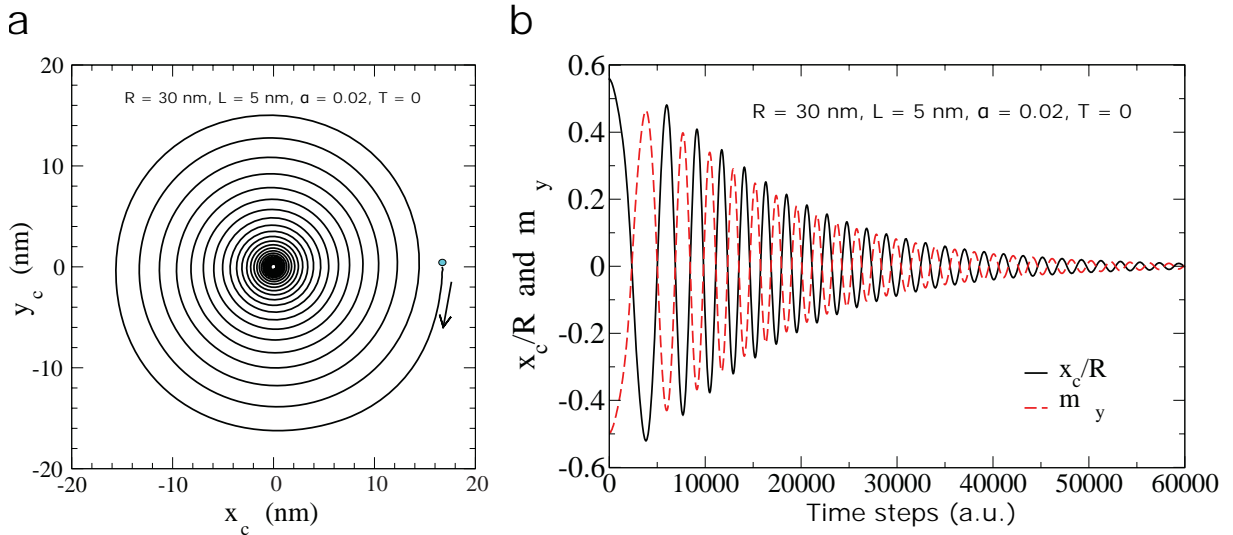
Figure 2.6: (a) Circular vortex gyration in a Permalloy disk after a displacement of 16 nm in the x-direction [11]. (b) Out of phase oscillation of the x-coordinate of the vortex core and the magnetization in the y-direction during the circular vortex gyration seen in (a) [11].

2.3   Ferromagnetic Resonance Modes in Disk Geometries

The physical phenomenon at the basis of the interaction between RF fields and vortex spin textures is ferromagnetic resonance (FMR). As evident from the first term in the LLG equation, magnetic moments precess around the axis defined by the externally applied field H_{ext}, sweeping out a cone at a certain angle θ. The frequency at which this precession takes place is the Larmor frequency and can be written as:

$$\omega_{Larmor} = \gamma |\mathbf{H}_{ext}| \tag{2.6}$$

Here γ denotes the gyromagnetic ratio and H_{ext} the externally applied magnetic field. When one introduces an alternating magnetic field perpendicular to the externally applied field, at specifically the Larmor frequency, the magnetic moment experiences resonance in which absorption of energy and angular momentum takes place. As a consequence, the magnetic moment now precesses around a modified angle θ'.

Two types of ferromagnetic resonance modes can be distinguished. The uniform mode describes the precession of all the magnetic moments at the same frequency and phase over the entire sample volume. However, in the case of higher order non-uniform modes, the moments can precess at the same frequency but with unequal phase, leading to the formation of spin waves. These are the spin analogy of phonons in which lattice distortions propagate through the solid in a wave-like fashion. A schematic representation of a one-dimensional spin wave is depicted in Figure 2.7.
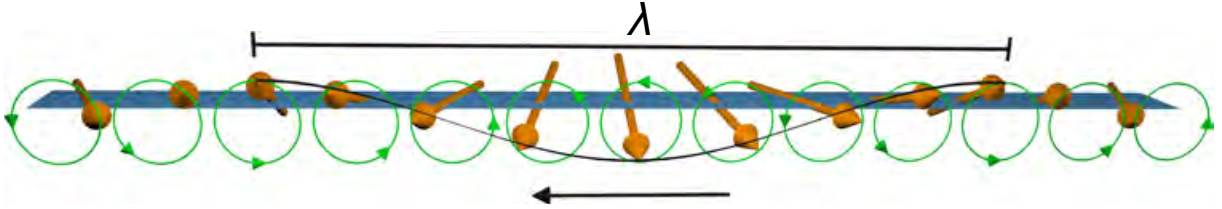
Figure 2.7: *Representation of a one-dimensional spin wave from Sluka et al. [12].*

Depending on the wavelength of the spin waves, they can be classified into dipole and exchange interaction dominated modes. The dipole interaction is longer ranged than the exchange interaction, and therefore dictates the behaviour of long wavelength spin waves. The exchange interaction governs the spin waves in the case of short wavelengths of the order of the magnetic exchange length. The dipole interaction induced magnetostatic spin wave modes can be further divided into the main groups depending on the relative orientation between the magnetization $\mathbf{M}$ and the IP wave vector $\mathbf{k}$. The group and phase velocity can have equal or opposite sign, resulting in positive or negative dispersions respectively. When the magnetization $\mathbf{M}$ and wave vector $\mathbf{k}$ are perpendicular, the corresponding dispersion is positive and the spin wave is referred to as a Magnetostatic Surface Wave (MSSW). The amplitude of this wave is maximum near the top and bottom surface boundaries of the sample and decays exponentially when moving inwards. When the magnetization and wave vector are co-linear, the spin wave is referred to as Magnetostatic Backward Volume Wave (MSBVW). This mode has a negative dispersion relation and propagates through the entire volume of the sample. The dispersion of the MSSW and MSBVW mode can be viewed in Figure 2.8a.

The nature of the different frequency behaviour of these modes can be explained by considering the stray field energy. For the MSBVW, the static magnetization and wave vector both lie IP. The dynamic magnetization on the other hand, can point perpendicular to the surface of the sample and gives rise to a dynamic stray field. After half the wavelength of the spin wave, this stray field reverses direction, resulting in a dipolar stray-field configuration (bottom of Figure 2.8b). The energy of this field lowers when the wavelength of the spin wave decreases (increase in wave vector), manifesting the negative slope in the dipole dominated part of the MSBVW dispersion.

a

b
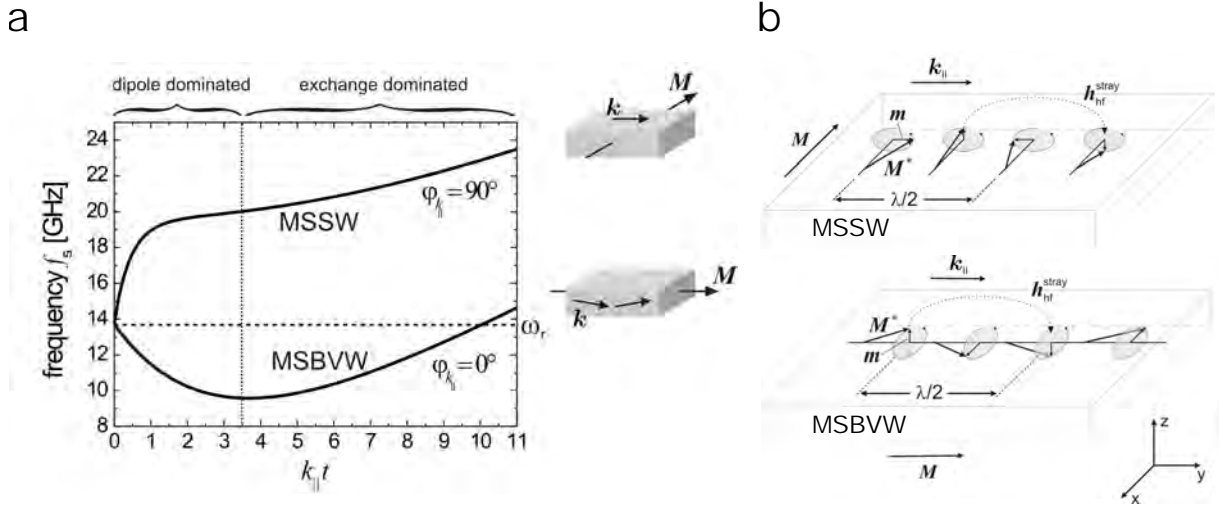
Figure 2.8: (a) Dispersion relation of the MSSW and MSBVW modes in the dipole and exchange dominated regimes [13]. (b) Stray field and dynamic moment alignment explaining the positive and negative slope in the dipole dominated regime for the MSSW and MSBVW mode respectively [13].

For the MSSW mode, after a distance of half a wavelength, anti-parallel dynamic moments can be found (top of Figure 2.8b). When increasing the wave vector (decreasing the spin wavelength), these anti-parallel moments approach each other and raise the energy of their dipolar field. This effect produces the positive slope of the dispersion of the MSSW modes. As the wave vector increases (to the point that $\mathbf{k} \sim 1/l_{ex}$), the exchange interactions starts to play a more dominant role, rendering the dispersion of also the MSBVW mode positive. The contribution of the exchange interaction is independent of the relative direction between static magnetization and wave vector and therefore effects the MSSW and MSBVW modes equally.

It is relevant to note the nature of spin waves in confined geometries. When reducing the dimensions of the ferromagnet, the boundary conditions modify the spectrum of the spin waves. When the size of the sample approaches the order of magnitude of the spin wavelength, standing spin waves can form (similarly to acoustic standing waves in drum skins). As generally the rule for mechanical standing waves, standing spin waves can only span the sample with an integer amount of half its wavelength. The scenario reduces to the treatment of a geometric well in which the formed standing wave has a wavelength of $\lambda = n * w/2$. Here n counts the amount of nodes and w represents the lateral dimension of the confining structure. In the dipolar dominated regime, the energy of the MSSW increases as the amount of nodes increases and its wavelength reduces, while the opposite is true for the MSBVW.

For these disk structure confinements, the occurrence of the stable ground state containing the vortex introduces multiple extra resonance modes, including standing spin waves. The three main resonance modes that can be induced are the gyrotropic mode at low frequencies (< 1 GHz) and two higher frequency modes (> 1 GHz): the azimuthal and radial modes. The former refers to the gyrotropic motion of the vortex core, while the two latter describe standing spin wave modes propagating through the spin texture of the vortex state along the azimuthal or radial direction respectively. These are the three main modes of interest and will be discussed in the following subsections.

2.3.1 The gyrotropic mode

In the case of gyrotropic resonance, the quasi-particle vortex gyrates through the sample geometry. The mode can be induced by applying an IP magnetic field pulse in the MHz regime or by spin-transfer torque [14]. This has been observed by time-resolved magneto-optical Kerr microscopy [15], time-resolved X-ray imaging [16, 17] and microwave absorption techniques [18]. Choe et al. [16] and Van Waeyenberge et al. [17] observed elliptical gyrotropic motion in rectangular Landau structures, while experimental features of the gyrotropic mode in circular nano-dots were observed by Park et al. [19]. The vortex core responds in two phases: initial acceleration during the field pulse and gyrotropic rotation after the field pulse [16]. It has come to light that the initial acceleration and rotation sense of the gyrotropic motion are not governed by the IP curling sense of the spin texture. In contrast with static magnetic fields, when dynamic fields are applied, the vortex does not move perpendicular but parallel to the external field direction. This can be understood by realizing that on a sub-nanosecond time scale, the dynamics are dominated by the magnetic moment precession around the field direction instead of damping [16]. Furthermore, when the magnetization of the core points OOP, the rotation sense of the gyrotropic motion is counterclockwise, independent of chirality. As explained by Choe et al. [16], this can intuitively seem like broken parity, but it is rather a simple and direct consequence resulting from initially defining magnetic moments and fields in a right handed coordinate system. The sense of rotation can be explained by taking into account the gyro-force: $\mathbf{F}_G = \mathbf{G} \times \dot{\mathbf{X}}$, arising from the gyrovector of the vortex. One can think of this force as analogous to the Lorentz force in which the vorticity q plays the role of electric charge. Also, while the vortex core undergoes gyrotropic motion, the magnetic structure of the core is deformed and this results in an enhanced magnetic core field.
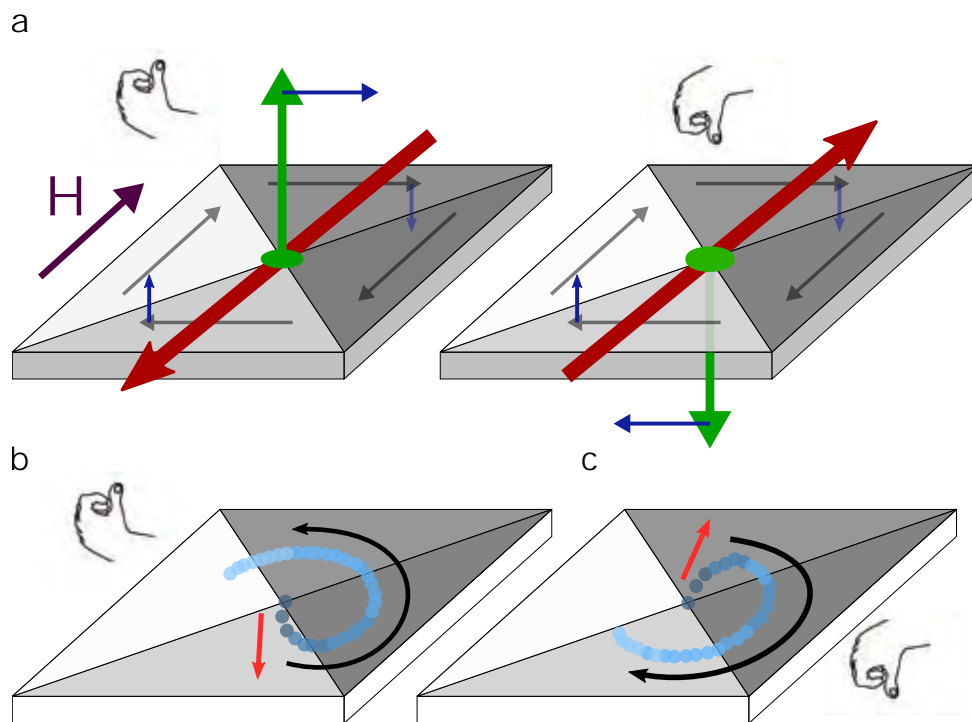
Figure 2.9: *Dependence of the initial vortex motion and rotation sense in the gyrotropic mode on the handedness and polarity respectively, as described by Choe et al. [16].*

Figure 2.9a displays the initial movement of magnetic vortices depending on the core polarity for Landau structures in LH and RH configurations illustrated by the hand pictograms. The gray arrows indicate the IP magnetization. The comparison to circular disks is straightforward. For a positive polarization (the left, green arrow), with an IP external magnetic field (purple arrow) pulse, the vortex moves towards the observer as displayed by the red arrow. The precessional torque generated by the external magnetic field is shown with blue arrows. Figure 2.9b and c represent the rotation sense (black arrow) and initial core acceleration direction (red arrow) in core-up (b) and core-down (c) states.

2.3.2 The azimuthal and radial modes

The radial and azimuthal modes can be understood in terms of dipole dominated standing spin waves. The wave vector of the radial mode lies perpendicular to the static magnetization direction and thus corresponds to the MSSW mode. The azimuthal mode propagates co-linear to the magnetization direction and is therefore a MSBVW mode. These radial and azimuthal spin wave modes can be elegantly described due to the cylindrical symmetry of the vortex state by counting the number of nodes n and m along the radial and azimuthal directions. The OOP component of the magnetization of spin waves can be described in polar coordinates using (equation 1 from Kammerer et al. [20]):

$$\Delta m_{z,n,m} = r_{z,n}(\rho) e^{im\phi} e^{-i\omega_{n,m,p}t} \tag{2.7}$$

The indexing ignores the permanent node present at the vortex core. The total number of azimuthal nodes equals $|2m|$, while the sign of m denotes the sense of rotation of the azimuthal wave (for CCW/CW m is positive/negative). The purely radial mode $(0,0)$ is excited most efficiently by an OOP magnetic pulse as reported by Buess et al. [21], while the lowest order azimuthal modes $(0, \pm 1)$ are excited by an IP field pulse. For larger disks, the vortex core is fixed at the center of the disk when the field strength of the magnetic pulse is insufficient and this leads to degeneracy of the lowest azimuthal modes $\omega_{n,m,-p} = \omega_{n,-m,p}$. When the disks have a smaller diameter, gyrotropic motion can be induced at smaller field strengths and this breaks the cylindrical symmetry, lifting the degeneracy of the azimuthal modes. In our system, the diameter of the disk is 1 μm and the thickness is 65 nm, giving an aspect ratio (thickness over radius) of 0.130, therefore a relatively large frequency splitting between the azimuthal modes is expected. Figure 2.10a displays several radial modes of NiFe disks with at the top the Fourier phase and at the bottom the Fourier amplitude for frequencies 2.8 GHz (I), 3.9 GHz (II) and 4.5 GHz (III). The top half of the disks represents the experimental data and the bottom part the simulation data. Figure 2.10b presents the single node azimuthal mode, occurring at 2.5 GHz with I (left) the experimentally acquired Fourier amplitude and (right) the Fourier phase. At the bottom (II), the temporal evolution of this mode is shown with a time interval of 80 ps between subsequent images.
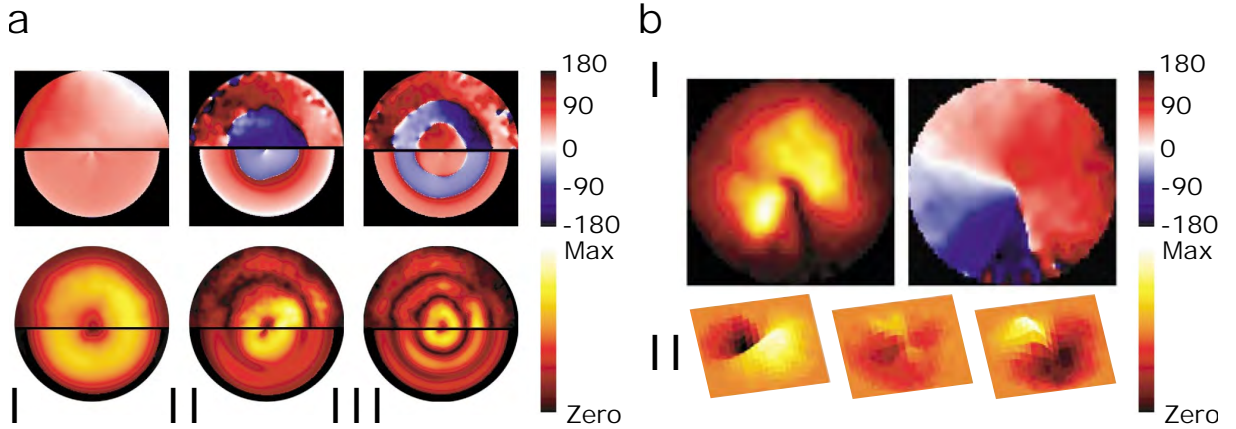

Figure 2.10: *Experimental and simulation examples of the radial (a) and azimuthal (b) modes adapted from Buess et al. [21].*
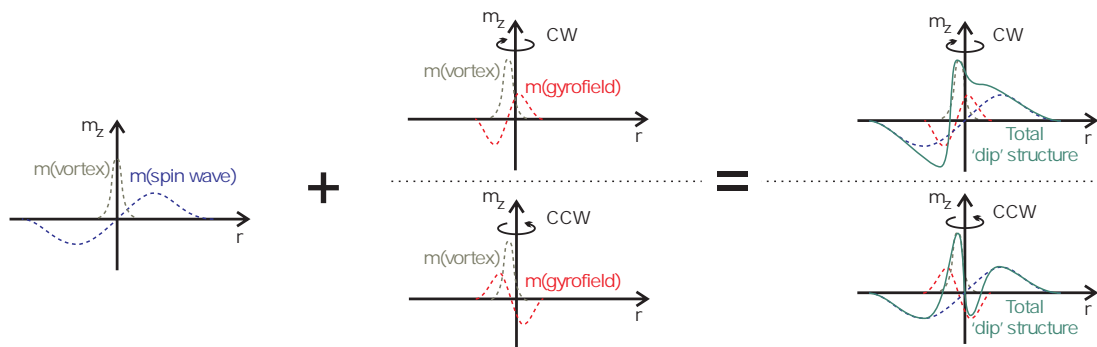
2.3.3   Magnetic vortex core reversal

The most promising usage of these modes, from a technological standpoint, is magnetic vortex core reversal in which the polarity is changed. This happens on a sub-nanosecond timescale and could therefore elevate the switching speed in electronic devices. This process generally proceeds as follows and can be viewed in Figure 2.11. The initial configuration is a right-handed vortex core (a). While the vortex core is distorted by the external rotating (b) field, an anti-vortex/vortex pair is created (retaining the total topological charge/vorticity q of the system) of opposite polarity (c-d). The initial vortex and anti-vortex attract each other and eventually annihilate (e-g), leaving a vortex with equal chirality but opposite polarity (h).
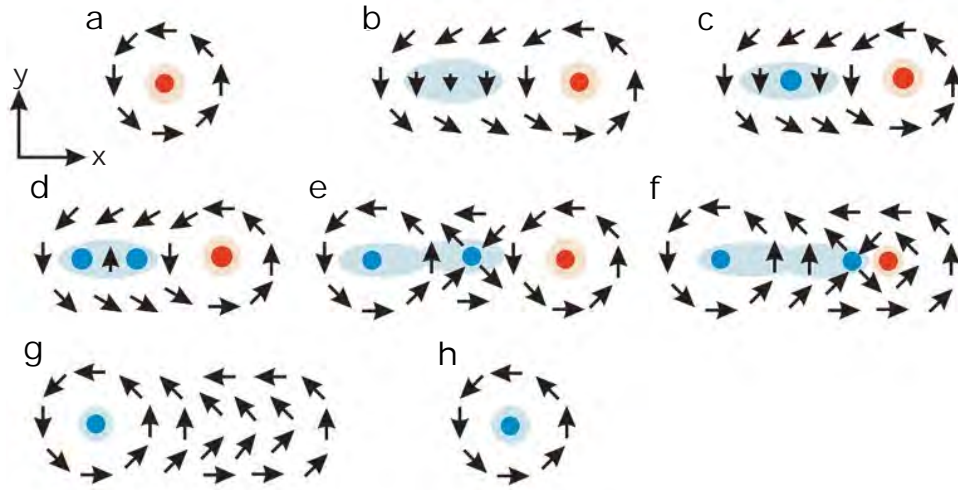
Figure 2.11: *The vortex core reversal process adapted from Van Waeyenberge et al. [17].*

The vortex/anti-vortex pair manifests itself as a distortion driven dip of opposite polarity formed close to the original vortex. This dip structure can be described by means of effective field theory, in which its origin is retraced to the gyrofield. The strength of this field is proportional to the velocity of the vortex core, which has led to the introduction of a critical velocity needed before vortex core reversal can be attained. But this notion has been challenged by Kammerer et al. [20]. They observed in the case of CW and CCW azimuthal spin wave induced core reversal, a wide range of core velocities from 100 m/s (CW) to more than 600 m/s (CCW). As is clear from their simulations, the nature of the formed dip structure differs depending on the rotation sense of the azimuthal spin wave excitation. For a vortex up state, a CW azimuthal mode generates a rotating vortex mode with equal rotation sense. This vortex movement in turn gives rise to the gyrofield, which acts constructively on the spin wave. The total interference of the magnetic z-components of the vortex, spin wave and gyrofield is a single dip structure as presented in the top right corner of Figure 2.12. Inversely, the CCW azimuthal mode and rotating vortex produce an opposite gyrofield, acting destructively on the original spin wave. This manifests itself in the double-dip structure as can be viewed in the right bottom of Figure 2.12.

Figure 2.12: *The dip structures formed during CW and CCW azimuthal spin wave induced vortex core reversal as described by Kammerer et al. [20].*

The reversal can for instance be achieved by applying IP or OOP field pulses. The hope of the micro-magnetic community was that the stable vortex state could encode logical information in the form of its polarity and chirality. In terms of gyrotropic mode switching, the vortex can switch polarity when the sense of rotation of the gyrotropic motion is equal to the chirality of the vortex spin texture. However, azimuthal mode switching can be achieved using rotating magnetic field with either sense of rotation. On top of this, azimuthal modes allow higher core switching critical velocities. Gyration induced vortex core reversal was accomplished by Van Waeyenberge et al. [17]) utilizing a continuous sinusoidal excitation field of 0.1 mT at 250 MHz to bring the vortex in gyration and a short IP field burst of equal frequency with an amplitude of 1.5 mT and duration of 1.4 ns triggering the core reversal. Azimuthal spin wave induced vortex core reversal was reported by Kammerer et al. [20] by applying rotating IP magnetic fields bursts of 24 periods long in a frequency range of $2.5 - 7.7$ GHz and amplitudes between $0.5 - 3.5$ mT.

2.4   The Basis of Micromagnetic Simulations

The objective of this section is to describe the basis of the micromagnetic simulations used in this thesis. The results of these simulations generally give a better understanding of the spin texture in the disk, enabling the qualitative explanation of several experimental results. Furthermore, it also functions as a good starting point for experiments. For instance, as will be seen in the result section, micromagnetic simulations can help determine the most suitable hole geometry/location in order to establish two stable ground states. It can in addition give us an estimation of suitable frequency and amplitude ranges to be excited in the CPW so that the vortex can be driven in a gyration mode or higher order spin wave modes. The simulations in this thesis are carried out with Mumax3 [22], the GPU-accelerated micromagnetic program that similar to the well known Objected Oriented MicroMagnetic Framework (OOMF), utilizes a finite element method in order to solve the LLG equation and integrate the result over the entire mesh using Runge-Kutta methods. The great benefit of GPU-based computation besides speed, is that it enables faster parallel computation, i.e. running multiple simulations simultaneously. An example of the discretized simulated disk with contacts that was used in the simulations is shown in Figure 2.13 below.

Figure 2.13: *An example of the disk structure with contacts used in the micromagnetic simulations. The color gradient shows the IP rotation of the magnetic moments, forming a vortex state.*

Stable states correspond to local/global minima in the free energy landscape. In terms of micro-magnetic simulations, this landscape is build up out of the relevant components mentioned in section 2.2.1. Mumax3 works towards finding these minima by keeping track of both the total free energy of the system and the time-evolution of the unit magnetization vector **m**. The total energy can arrive at the noise floor of the simulation, rendering the energy parameter as a means of minimizing the total energy unusable. Therefore the program switches to monitoring the derivative of the magnetization vector instead. The minimum rate of change that corresponds to an energy minimum can be given as an input, allowing control over the rigorousness/validity of the ground state. Generally, in our simulations, the maximum allowed rate of change of every cell is set to 10^{-8} rad before a ground state is achieved with a significant degree of confidence.

This leads to the relevance of setting correct dimensional values for the cells in the mesh. A compromise between accuracy and computation time needs to be made here, since a smaller cell size leads to more accurate results, but drastically increases the computation time. Therefore the lateral dimensions were chosen to be of the order of the magnetic exchange length, the characteristic length scale over which magnetic moments feel the exchange field of their neighbours, and as a result change their alignment. For Cobalt, this length is approximately 5 nm and is used as the order of magnitude for the length of the cubic cell edges. It is important to realize that setting the cell size much larger than $l_{exchange}$ will result in unphysical behaviour of the system. Another point worth mentioning is the role played by magnetic anisotropy and the plausible existence of a magnetic easy-axis. The films under consideration are fabricated using sputtering, which produces a highly poly-crystalline configuration. However, since Cobalt does not have strong magnetic anisotropy, all directions can be considered to be equal and the anisotropic energy does not need to be taking into account by setting the anisotropic constant to zero. Furthermore, we utilize the Cobalt parameters: Gilbert damping $\alpha = 0.01$, Magnetic saturation $M_s = 1.4 \times 10^6$ A/m and exchange stiffness $A_{ex} = 30 \times 10^{-12}$ J/m.

2.5   Co-planar Waveguides for Oersted Field Generation

CPWs are commonly used in microwave-based applications. It utilizes different conductive and dielectric materials in restricted geometries in order to confine electromagnetic waves in one or two spatial directions, leading to an uniform propagation in one single direction. A CPW consists out of a transmission line (with width w) and on both sides ground planes, leaving trenches (of width s) disconnecting the transmission line from the ground planes. The two most significant features for our experimental goals are a broadband transmission and uniform field strength above the transmission line of about $10 - 100$ Oe. In order to achieve broadband transmission, 50 Ohms impedance matching between the CPW and external lines is crucial. Loss in signal results in a reduced current density in the transmission line, leading to a reduced field strength. The geometric constants of the design, w and s, have significant influence on the impedance of the CPW and therefore on the loss. Suitable values for these geometric constants have been determined using an online CPW impedance calculator [23], resulting in $s = 5.3$ μm for $w = 8$ μm. A current I flowing in a CPW generates a magnetic field distribution **h** of the Oersted field. In vacuum ($\mu = 1$), the field distribution can be approximated using the Karlqvist equations [24]:

$$h_x(x,y) = \frac{1}{\pi}h_0 \left(\arctan \frac{y + \frac{w}{2}}{x} - \arctan \frac{y - \frac{w}{2}}{x} \right) \tag{2.8}$$

$$h_y(x,y) = \frac{1}{2\pi}h_0 \ln \frac{(y + \frac{w}{2})^2 + x^2}{(y - \frac{w}{2})^2 + x^2} \tag{2.9}$$

where $h_0 = \frac{I}{2w}$ in the infinitely thin sheet thickness approximation. To take into account the flow accumulation due to the skin effect, the current profile perpendicular to the flow direction was taken to follow: $j(y) = C[1 - (2y/w)^2]^{1/2}$, where C defines the current density in the middle of the transmission line [13]. Figure 2.14a and b display a schematic representation of a CPW (with field lines) and the field distribution as described by the Karlqvist equations respectively.

a

b
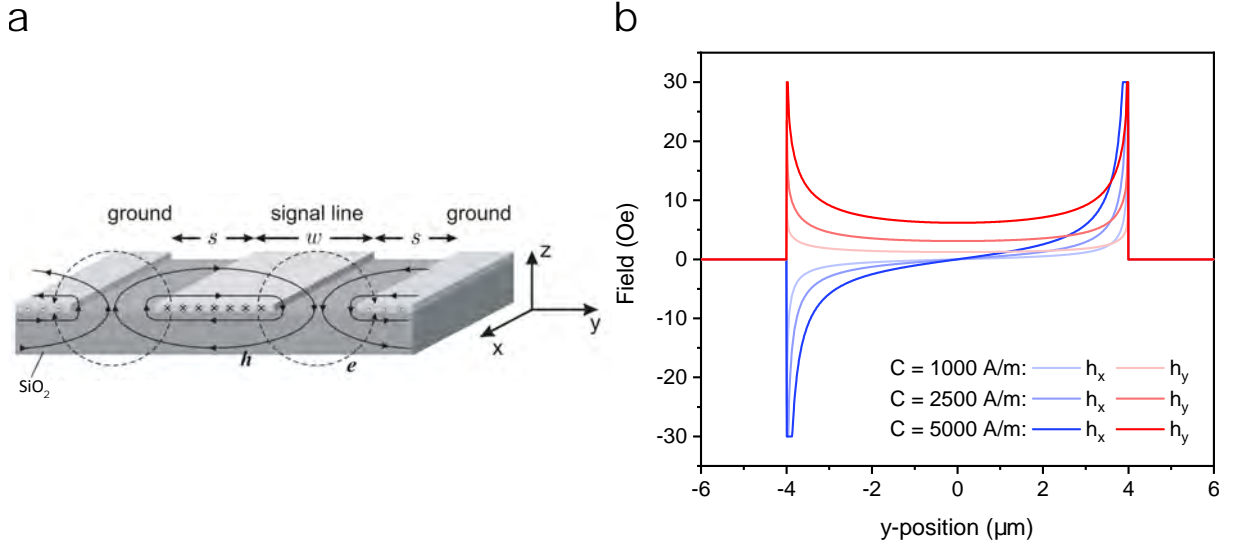
Figure 2.14: *(a) Schematic presentation of the geometry and field lines in a CPW from Neudecker et al. [25]. (b) The Karlqvist equations, equation 2.8 (blue) and 2.9 (red), for different central current densities (C) along the width of the transmission line.*

Now that a theoretical framework for both the triplet superconductivity, junction mechanics and ferromagnetic resonance modes has been established, the following chapter can proceed with the used methods in this project.

CHAPTER 3

Methods

This chapter gives a detailed description of the sample fabrication steps. It is divided into: the CPW fabrication, the fabrication of the Co/Nb disks on the CPW and the modified milling steps used to complete the structures on the CPW minimizing damage to the stripline.

3.1   Sample Preparation

The fabrication steps of the CPW and subsequently of the Co/Nb disks on the CPW are described in this section, but first the common procedures are mentioned. All samples were prepared on Si wafers with a 300 nm thermal oxide layer of SiO_2 and lateral dimensions of 0.5×0.5 cm. Necessary ultrasonication cleaning steps with both the solvents acetone and isopropanol were undertaken before the e-beam resist was spin-coated. First a layer of 400 nm thick 600K PMMA was spin-coated for 1 minute at 2000 RPM. Afterwards, the resist was baked at 150 degrees Celsius for 3 minutes. An additional layer of 250 nm thick 950K PPMA was spin-coated and baked in the same manner. Using this two-resist recipe results in the desired undercut after exposure and development, enabling a more successful lift-off. E-beam lithography was performed in a Raith set-up, utilizing exposure parameters corresponding to a 10 nA spot size and dosages of 360 μC/cm^2 for finer features and 300 μC/cm^2 for larger areas. After exposure, standard development in MIBK was accomplished and the result was checked under the optical microscope.

3.1.1   CPW fabrication

Since the subsequent accurate alignment of the disks on the transmission line is important, alignment marks are added in the e-beam design. These can be used for a three-point alignment when patterning the disk design on the waveguide. The finest and most important feature, the transmission line with trench, was patterned with a lower beam current, smaller spot size and smaller step size, enabling the completion of more accurate patterns. To reduce the patterning time, the larger structures of the waveguide were written with a higher beam current and larger step size. After development (Figure 3.1a), the waveguides are loaded in the thermal evaporator. Here a sticking layer of Cr with a thickness of approximately 5 nm was deposited at a growth rate of ~ 0.2 Å/s, before 100 nm Au was deposited at a growth rate of ~ 2 Å/s. To finalize the CPW, the sample was immersed in acetone and slight ultrasonication was used to stimulate the lift-off process, giving rise to the CPW as displayed in Figure 3.1b. The width of the stripline and trench were specifically chosen to be 8 μm and 5.3 μm respectively, resulting in sufficient impedance matching with exterior connections and therefore reduced signal loss. In a separate sputter system (the Z400), a 100 nm SiO_x layer is deposited at a sputter rate of 3.55 nm/min. This ensured the absence of electrical shorting between the CPW and disks and also reduces the chances of damaging the stripline while the disks are milled.
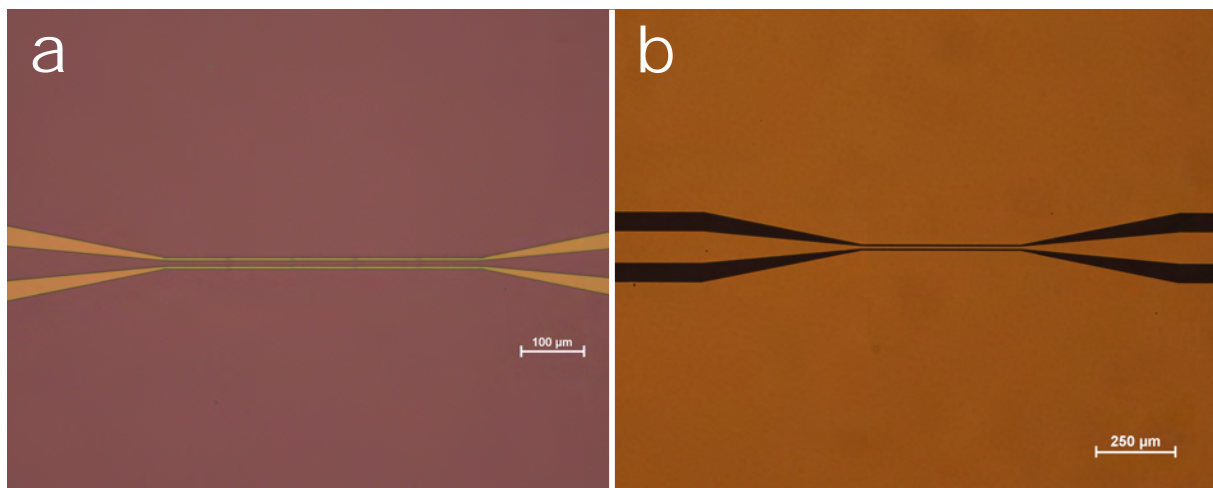
Figure 3.1: *(a) Pattern of the CPW before deposition. (b) The CPW after deposition and lift-off.*

3.1.2 Co/Nb disk fabrication on the CPW

Now the focus is shifted to the fabrication of the Co/Nb disks on the CPW stripline. Identical spin-coating procedures were undertaken as previously mentioned before placing the sample in the lithography system, with the exception of an additional layer of electra to prevent charging effects and allow for better alignment. Important in this step is the alignment between stripline and the structure of the design that will be milled into the disk with trench. Favourably, this structure is placed in the middle of the stripline, so that the Co layer experiences an uniform IP rotating field. This was accomplished by using a three-point alignment method available in the Raith set-up. The finer features, the structures on the stripline, were patterned with dosage of 360 $\mu C/cm^2$, while the contact lines and pads were written with a dosage of 300 $\mu C/cm^2$. This was followed by standard development procedures and a check under the optical microscope, ensuring correct alignment was achieved. On the CPW, three disk structures are fabricated on the stripline and 8 dummy structures are placed on the ground planes close to the stripline. These dummy structures are used to fine tune the parameters used during focused ion-beam (FIB) milling. The substrate with disk pattern is then placed in a UHV sputter system for the deposition of Co and Nb. Firstly the 65 nm thick Co layer is sputtered utilizing an argon plasma at a pressure of 4.0×10^{-3} mbar, in which a sputter rate of 4.48 nm/min is achieved. Secondly, the 45 nm thick Nb layer is sputtered under similar circumstances at a sputter rate of 3.13 nm/min. As a last step of the deposition process, the sample is taken out of the UHV sputter system and placed in separate HV sputter system for the deposition of 7 nm Pt or Au. This layer serves as a capping layer and protects the disk from oxidation and damage that could be introduced by the Ga ions during milling. The whole sample is once again immersed in acetone for lift-off. The sample is finalized by nanostructuring the structure into a disk by FIB milling in the Helios Dual Beam system and by introducing the trench, giving rise to the two Nb contact pads and the Co weak link.
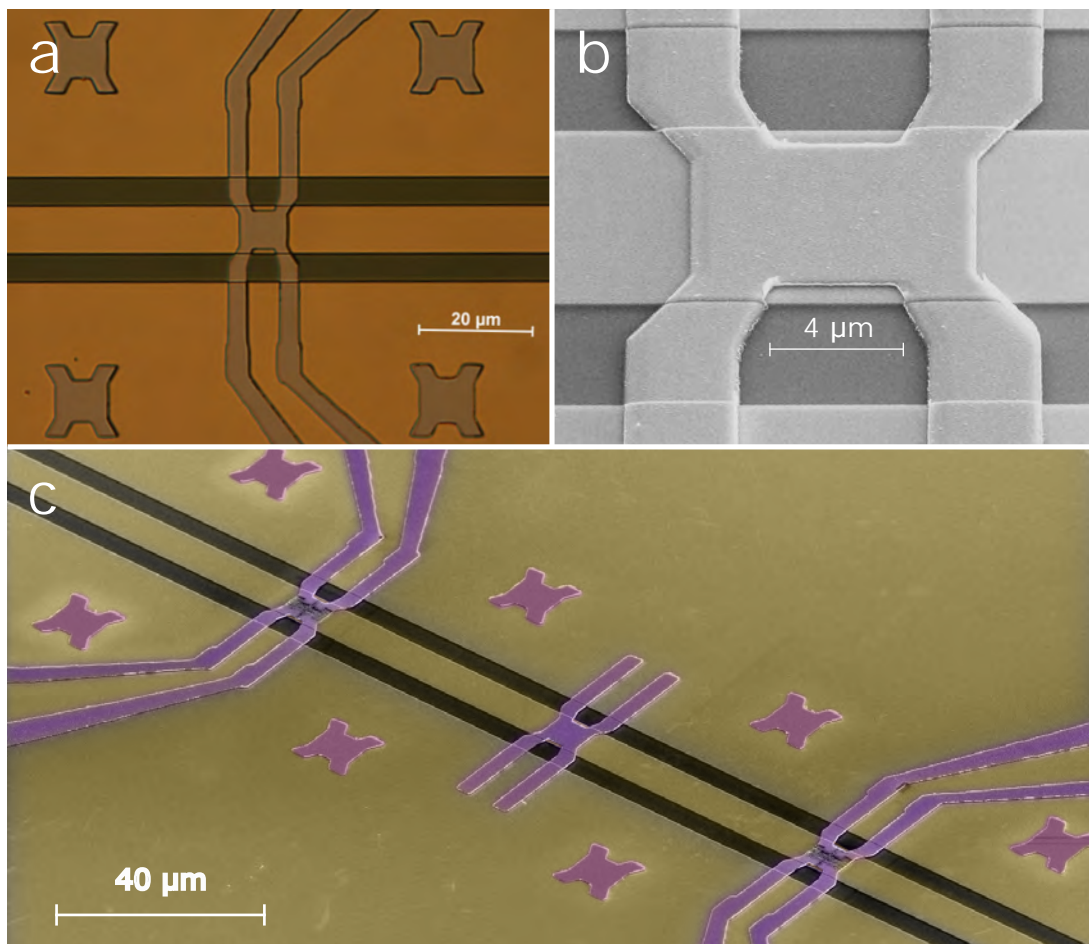
Figure 3.2: *(a) The pattern of the structure aligned on the stripline. (b) Co/Nb layer on the stripline, ready for milling. (c) A false colour scaled SEM image showing the three samples (purple) on the stripline (gold) and the 8 dummy structures (purple). Upon closer investigation, one can see the effect of FIB milling on the left and right samples on the stripline.*

3.1.3   The modified FIB steps

The FIB steps for conventional disks not placed on a CPW are slightly different compared to the ones on a CPW. As seen in the false colour scaled image in Figure 3.3a, the bilayer of Co/Nb (purple) is aligned in the middle of the transmission line of the CPW (gold). A significant part of this bilayer area will be milled away, leaving the disk in the center of the transmission line where an uniform IP field at excitation will be present (see Figure 2.14b). The most important point to be made here is the possibility of damaging the waveguide. The milling of amorphous materials deposited with sputtering can be non-uniform, leading to certain parts being milled faster than others. The 100 nm silicon oxide layer does not only disconnect the CPW and disk electronically, but also protects the CPW from getting damaged in the FIB procedure. In the first FIB step (Figure 3.3b), large areas are milled. The selected areas for milling do not tolerate any overlap with the CPW and therefore the edge is left un-milled. To disconnect the contacts, a small linecut (displayed in light blue) is made, damaging the CPW minimally and locally.
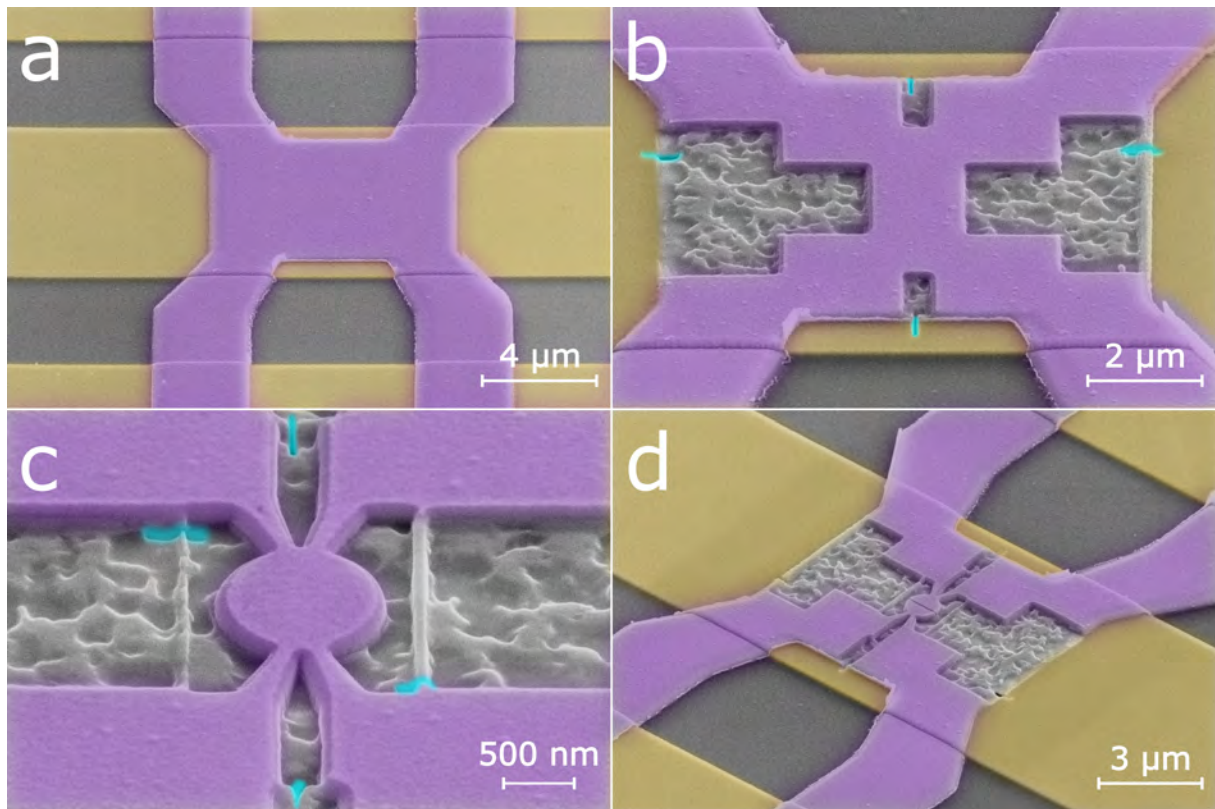
Figure 3.3: *(a) Rectangular bilayer region aligned in the middle of the transmission line of the CPW, ready for milling. (b) First FIB step, displaying the necessary linecuts in light blue. (c) Finer milling step, resulting in the disk geometry. (d) Finalized disk structure with trench.*

The same is done when milling the finer parts of the disk (Figure 3.3c). These small line-cuts are not expected to influence the uniform current distribution in the CPW under the disk significantly. In the final step, as with the conventional disks, the trench is milled leaving the finalized disk structure (Figure 3.3d). The next chapter is dedicated to the experimental results acquired on disks on substrates (static disks with/without holes) and disks on CPWs (dynamic disks).

Results and Discussion

The results and discussion chapter is divided into four main passages: micromagnetic simulation results, CPW simulation results, progress on the experimental setup and experimental results. The micromagnetic results are acquired, as previously mentioned, using Mumax3. These mainly focus on the occurrence of the gyrotropic mode in the disk structures. The simulation results on the waveguides are obtained using the electromagnetic software package Sonnet Pro. The experimental setup was mainly changed with regards to the RF setup needed to excite ferromagnetic resonance modes in the disk through the waveguide. Finally, the experimental results treat static (larger disks and disks with hole geometries) and dynamic (disks on the CPWs) samples.

The motivation for these sections is as follows. The micromagnetic results give an indication for the range of field strengths needed to induce FMR modes. The CPW simulations gives insight on suitable designs and the range of the field strengths that can be physically generated at certain frequencies. The progress on the setup shows the steps taken to reach sufficient FMR excitation. And finally, the experimental results detail the current standing regarding the static and dynamic disks. They also fortify the promises of using these devices for long range spin triplet generation and as non-volatile superconducting memory .

4.1 Mumax3 Simulation Results

4.1.1 The magnetic phase diagram of Co disks

In the future the geometry of the devices might be altered significantly and it is important to know if the vortex configuration is still a stable ground state in the modified structure. For a specified material, the aspect ratio (given by thickness over radius) influences the magnetic phase of the structure. Since most of the literature on micromagnetic simulations and experimental magnetic nano-structures investigates the soft magnetic material Permalloy (Py), NiFe, the exact magnetic phase diagram of Cobalt cylinders was unknown. Most interesting to us is the stability and region of the stable magnetic vortex. Figure 4.1a shows the phase diagram for Py taken from Novais et al [26], and the right one for Co, with the reduced radius (with respect to the exchange length) on the x-axis and the reduced height on the y-axis. Here, the exchange length of Co is taken to be ~ 5 nm.

a   b
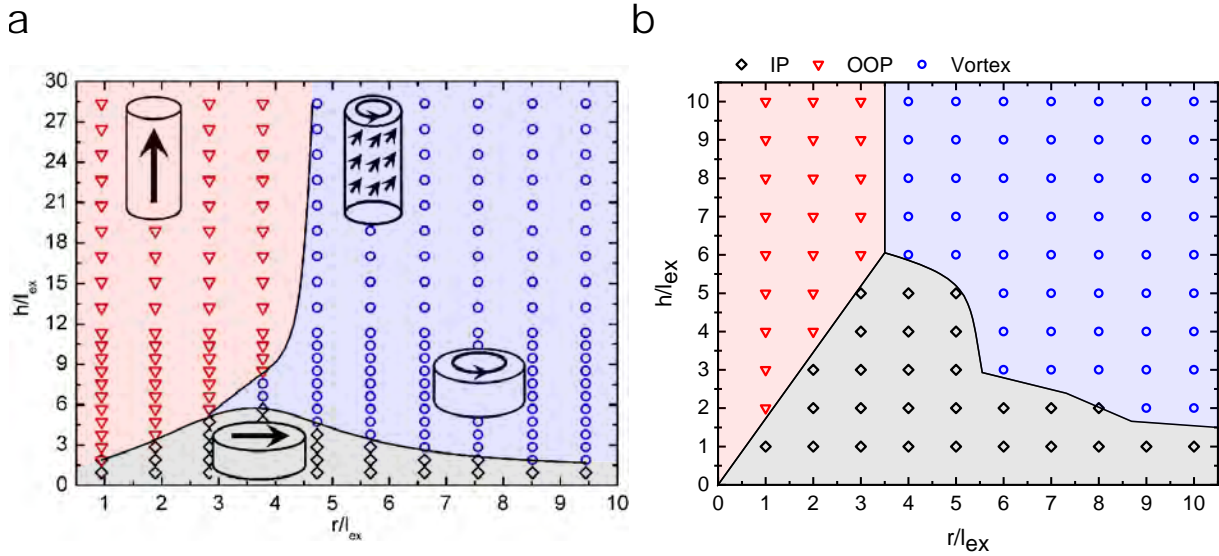
Figure 4.1: *(a) The magnetic phase diagram of Py disks displaying the different possible ground states for a range of aspect ratios adapted from [26]. (b) The magnetic phase diagram for Co disks simulated during this project.*

Three regions can be distinguished: OOP magnetization, IP magnetization and the vortex state. For the OOP state the curved boundary of the cylinder dominates the magnetostatic interaction and forces the moments along the length of the cylinder. For the IP magnetization the magnetostatics of the circular top and bottom plane of the cylinder dominates and forces the moments IP. When a suitable balance between the two magnetostatic components is reached, a vortex state appears for certain aspect ratios. Every data point in Figure 4.1b was obtained by relaxing the specific system in three different initial conditions: random, OOP and IP magnetization along the x-axis (for circular disks any IP axis will do). The total energy of the relaxed states was compared and the lowest energy state was coined the ground state for that geometry. For certain aspect ratios close to phase boundaries, the configuration is more likely to get trapped in a local minimum in the energy landscape. For this reason, some simulation points were also initialized in a vortex state to enable convergence to the global minimum. Vortex states close to the OOP boundary generally have a significant enlarged vortex core and can have an OOP component through the entire structure. As Figure 4.1b (and the theoretical phase boundaries) motivates, the disks with an aspect ratio of 0.13 ($h = 65$ nm, $r = 500$ nm) are well into the stable vortex ground state regime and apart from the vortex core, no OOP magnetization is present in these geometries.

The phase diagram of Py and Co are slightly different due to the deviation in magnetic properties of the two materials (exchange stiffness, saturation magnetization etc.). Interestingly, the phase diagram of elliptical soft magnetic materials can harbor two magnetic vortices of opposite chirality [26]. For specific aspect ratios, these asymmetric structures can switch between one or two vortex states by applying the field along the long or short axis. In the future, these two states in elliptical disks will be investigated with regards to their use in superconducting memory. In the next section however, the conventional disk slightly modified by the introduction of a hole is inspected for the same purpose.

### 4.1.2   Ground states of disks with hole geometries

Essential for superconducting memory utilizing spin triplets is the switchability between two magnetic configurations that are stable at zero field. Disk with hole geometries can harbor these two stable magnetic ground states at zero external field: one with the vortex in the center of the disk (Figure 4.2a) and one with the vortex pinned in the displaced hole (Figure 4.2d) [27]. When sweeping the field in the y-direction, the core is moved closer or further away from the hole (depending on the chirality of the vortex state). At a certain field strength, the core pins to the hole and the OOP component disappears (Figure 4.2b). Continuing the sweep with increasing field strengths causes the core to nucleate on the other side of the hole (Figure 4.2c). Sweeping back to zero field moves the core back towards the hole until it re-annihilates. However, this time at zero field (Figure 4.2d), the core maintains pinned to the hole. Here, the stability of these ground states in different geometries is inspected.
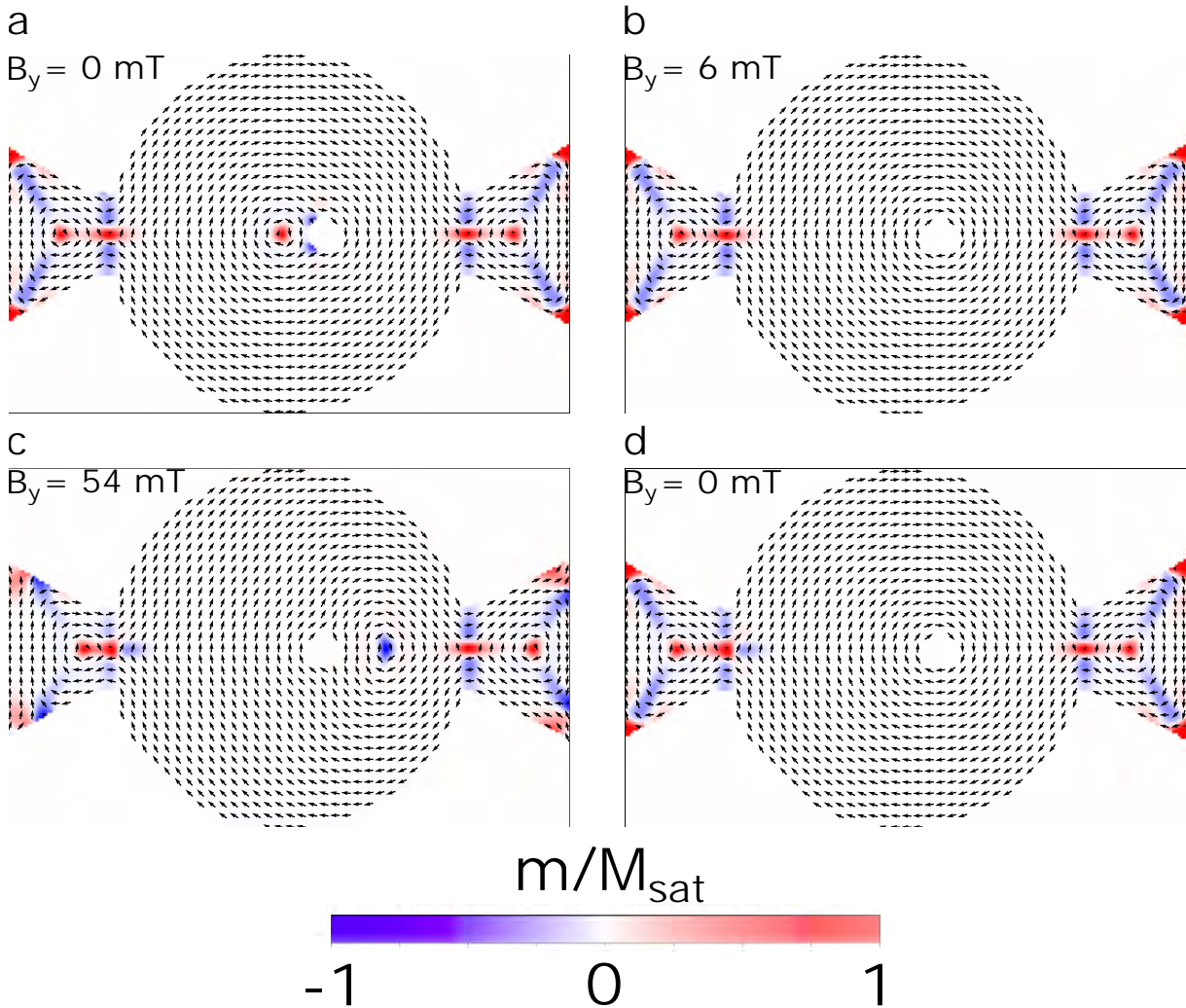
Figure 4.2: *(a) Initial state of a disk with a diameter of 1 μm and a hole with a diameter of 96 nm displaced 100 nm from the center of the disk. (b) At $B_y = 6$ mT, the vortex annihilates into the hole until at $B_y = 54$ mT (c) the vortex nucleates at the other side of the hole. (d) When sweeping back to 0 mT, the stable state leaves the vortex pinned to the hole.*

Depending on the geometry of the disk and the initial state from which the structure is relaxed (complete OOP/IP saturation), the vortex ends up pinned or depinned from the hole as the starting configuration. The magnetic vortices in the contacts are artificial and are not expected to be present in the physical sample. They from due to the abrupt boundary on the left and right side of the sample. When sweeping the field too far (~ 60 mT), the interaction of the central vortex with the vortices in the contacts leads to the deformation of the true vortex and unphysical configurations of the spin texture. Also, as can clearly be seen by comparing Figure 4.2a and c, the vortex can change its polarity when reemerging from the hole.

Furthermore, the stability of the two ground states can be inspected by looking at the energy profile when sweeping the field in the y-direction. This was done for different disk diameters and placements of the hole. The dark/solid and lighter/dashed traces represent the up and down sweep respectively.
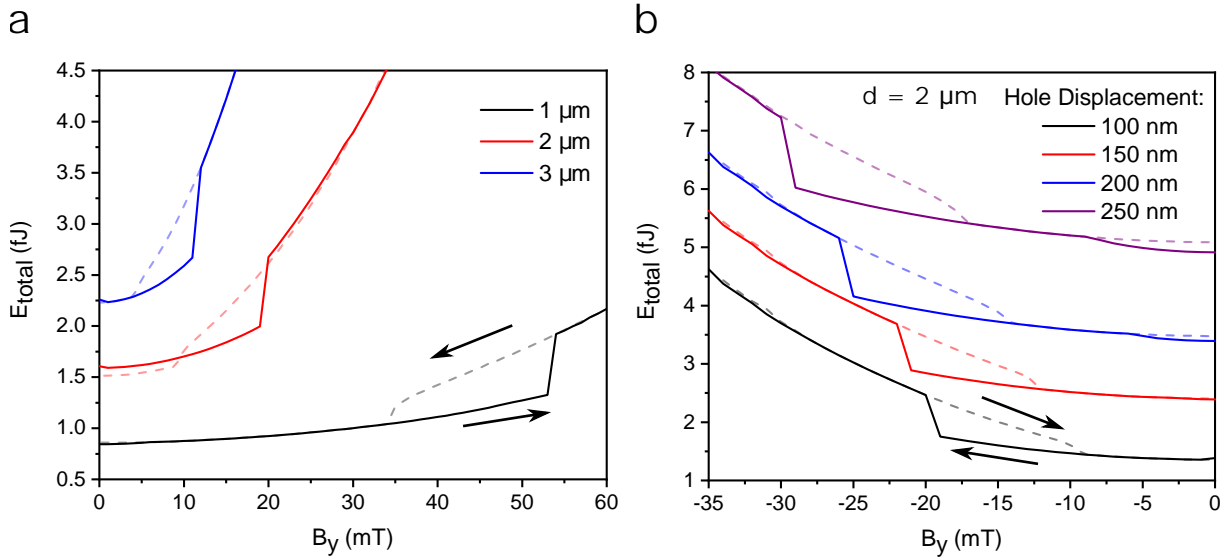

Figure 4.3: *(a) Total energy profile for disk structures with a 96 nm diameter hole displaced 100 nm from the trench for three different disk diameters. The energy difference between the two zero field states is the most significant in the 2 μm disk. The black arrows indicate the sweep direction. (b) Here the hole is increasingly displaced to the right from the middle of the 2 μm disk. The energy difference between the two states is enlarged for increased displacements. The traces are displaced vertically in order to visualize the trend better.*

Figure 4.3a makes clear that the 2 μm disk is suited for vortex pinning and depinning for the creation of two stable zero field states. For larger disks, the vortex becomes more mobile and annihilates/nucleates at lower field strengths. The simulation data plotted in Figure 4.3b was acquired on a vortex state with opposite chirality and therefore the annihilation/nucleation of the vortex at the hole on the right side happens at negative fields. When displacing the hole further to the right of the center of the disk, the energy difference between the ground states increases. Although, when the hole is displaced too far to the right, the vortex remains depinned from the hole at zero field for both sweep directions. This was observed at a hole displacement of 300 nm.

The next section elaborates on the FMR excitations in the Co disk. Strikingly, this oscillating RF fields can make the vortex pin and depin from the hole [27]. They can also induce long range FMR modes for which the focus is on the gyrotropic mode.

4.1.3 FMR excitations in the Co disks

Mumax3 can furthermore give insight in the FMR mode spectrum of the Co disk and which oscillating field strengths are needed for sufficient excitation. A general method to obtain this spectrum is to excite the structure with a block wave pulse of several mT strength. The m_z oscillation over one half of the disk forms the time signal which is Fourier transformed. The main contribution to the oscillation will be the vortex core appearing in and disappearing out of the region under consideration. If one would take the signal of the entire structure into account, the contribution of the gyrating vortex core will form a constant offset and no clear gyration frequency will be obtained. As can be seen in Figure 4.4a, the disk of 1 μm diameter is excited with four different pulse strengths for 200 ps. The initial data of the signal is quite hectic due to the distortions coming from the pulse. To filter this from the spectrum, the starting point of the signal is chosen to be a point where the steady decline of the oscillations becomes apparent. Therefore, the Fast Fourier Transform of this time signal is taken between 10 ns and 36 ns.
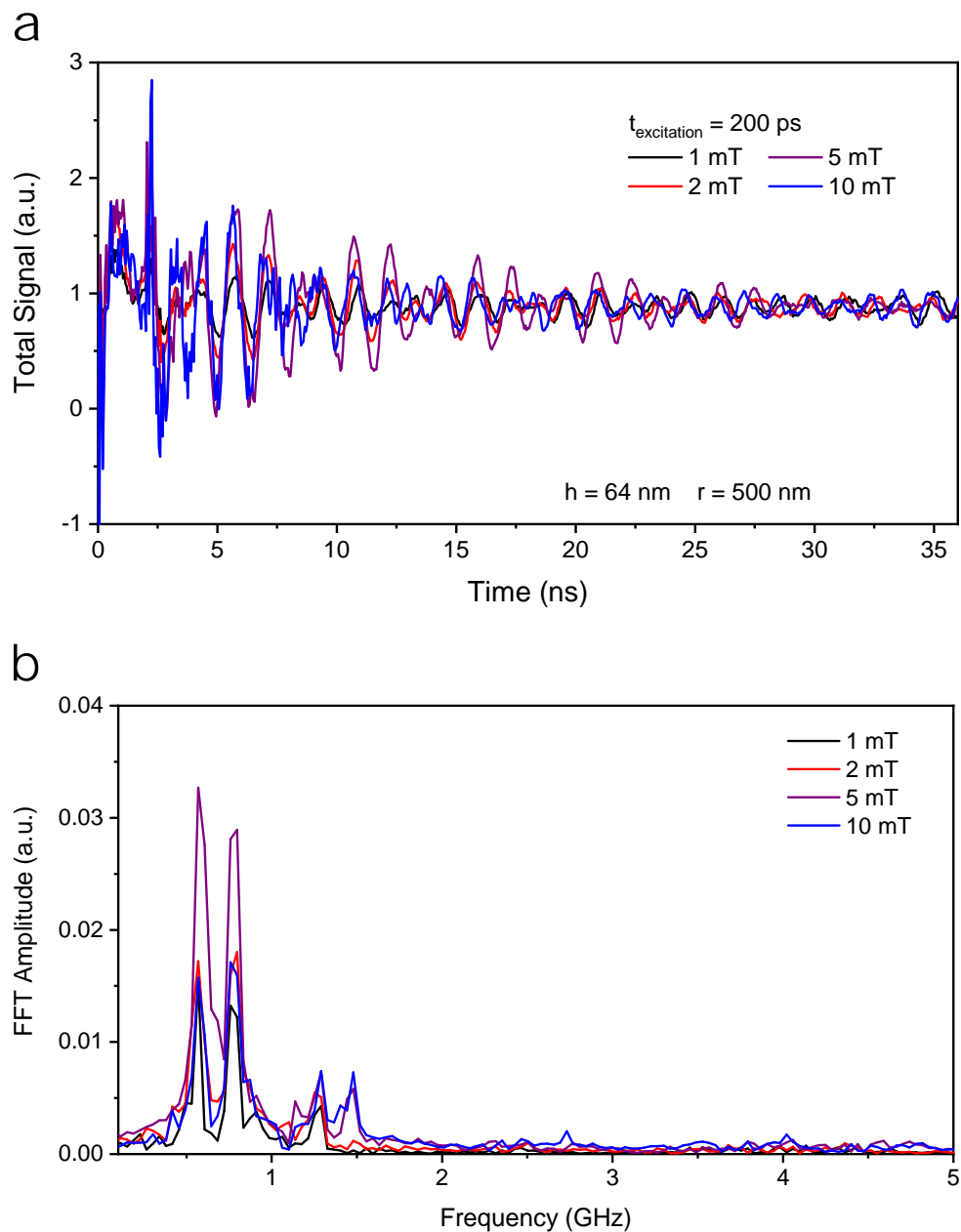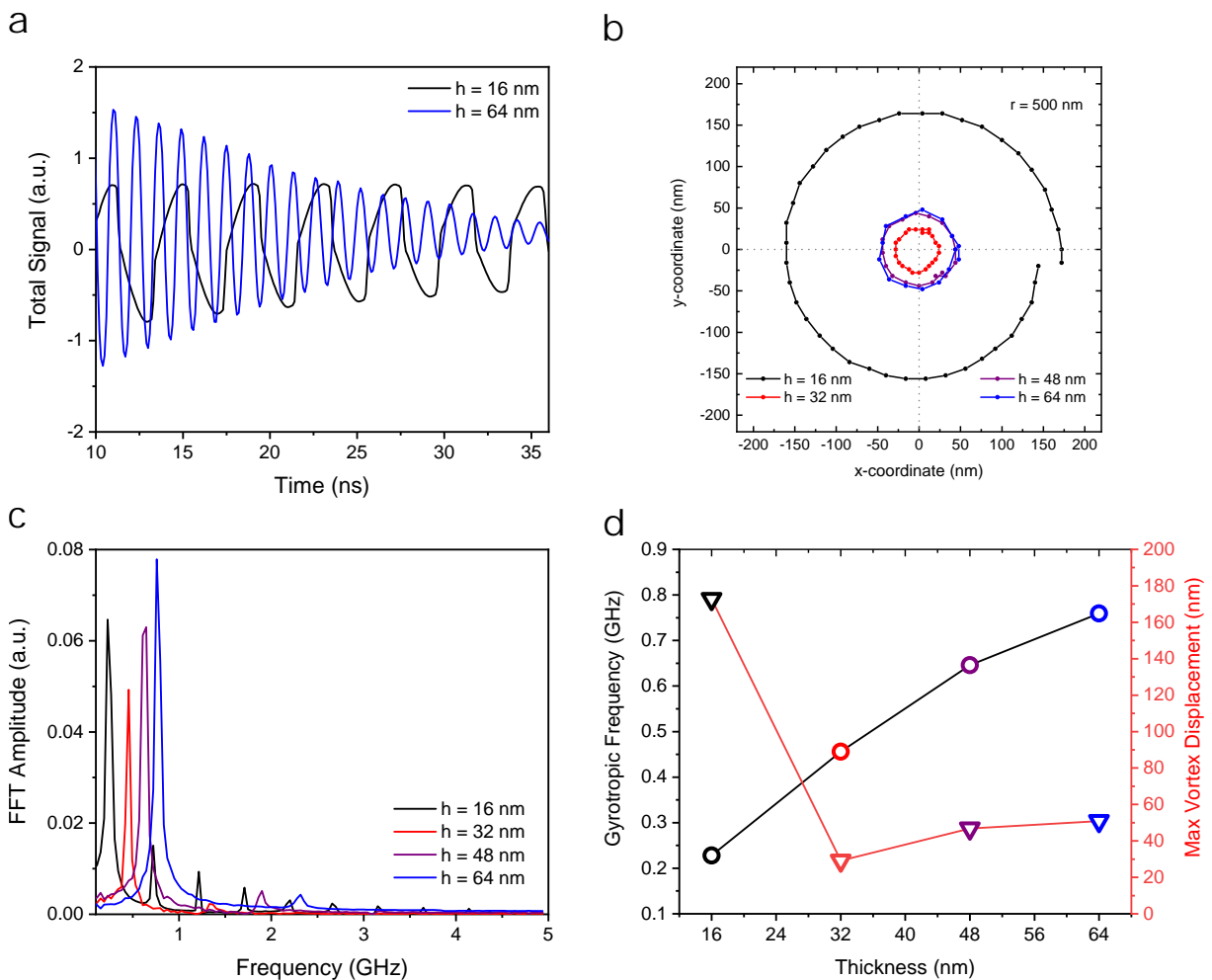

Figure 4.4: *Time signal of the m_z oscillations of the right half of the disk (a) and its frequency spectrum (b) after a blockwave pulse of 200 ps for several field strengths.*

As clear from Figure 4.4b, the gyrotropic frequency splits in two distinct values, caused by the broken geometric symmetry due to the presence of the contacts [27]. Furthermore, the 5 mT pulse couples better to the disk than the 10 mT pulse. This is hypothesized to be caused by the interaction of the central vortex core and the vortex core in the contacts of the disk when the trajectory of the central core comes to close to the contacts. However, the vortices in the contacts are artificial and form as a result of the abrupt boundaries at the end of the contacts. Nonetheless, the frequency spectrum shows approximately the same gyrotropic frequencies for different field pulse strengths, although the trajectory of the vortex core movement is enlarged. This indicates that the vortex core velocity reaches an increased maximum value when the pulse strength is elevated.

The trajectory of the vortex gyration is rather small, which indicates a limited change of the overall spin texture in the disk. The field strength can straightforwardly be increased for more substantial vortex gyration, although this might turn out to be difficult to achieve experimentally. For this reason, other pathways to enlarge the trajectory are explored.

### 4.1.4 Geometric tuning of the gyrotropic mode

One way to enlarge the vortex gyration trajectory is by tuning it with the geometry of the sample. The geometry of the disk has a significant effect on the gyrotropic mode. Specifically, the vortex mobility can be altered by changing the thickness or radius of the samples. Here, an elevated trajectory distance of a single core rotation around the center of the disk is equalized to a more significant change in the spin texture gradient. Tuning the geometry suitably, lower Oersted fields could attain the needed spin-texture change to observe the effect of the gyroptropic mode on the critical current. This way, one can compensate for the loss through the waveguide. Figure 4.1b indicates that the geometry is well into the vortex regime, meaning that the thickness and radius can be significantly modified while maintaining the stable vortex ground state. In these simulations, the contacts are neglected since the interest is mostly focused on the general behavior of the magnetic structure. First the effect of changing the thickness of the disk on the gyration mode is investigated, while the radius is kept constant at 500 nm.

Figure 4.5: *Time signal of the m_z oscillations of the right half of the disk for different thicknesses (with a constant radius of 500 nm) (a) and the core trajectory of the first oscillation (b) after a blockwave pulse of 200 ps for 5 mT field strength. (c) The frequency spectrum of the m_z oscillations shown in (a) and the gyrotropic frequency and maximum vortex displacement as a function of thickness (d).*

Reducing the thickness results in an abrupt higher mobility of the vortex core (Figure 4.5b) when reaching a thickness of less than 4 times the exchange length. The gyrotropic frequency (the large peaks in Figure 4.5c and black trace in Figure 4.5d) is furthermore continuously decreased when reducing the thickness. Experimentally changing the height of the sample is a modification that can easily be achieved. However, the likelihood of cutting through the Co disk when milling the trench does become more plausible for thinner samples. The features in the frequency spectrum above 1 GHz are indications of higher order modes.

Enlarging or reducing the radius will have a substantial effect on the vortex mobility as well. Figure 4.6a displays the m_z oscillations of the right half of the disk for different radii and a thickness of 32 nm.
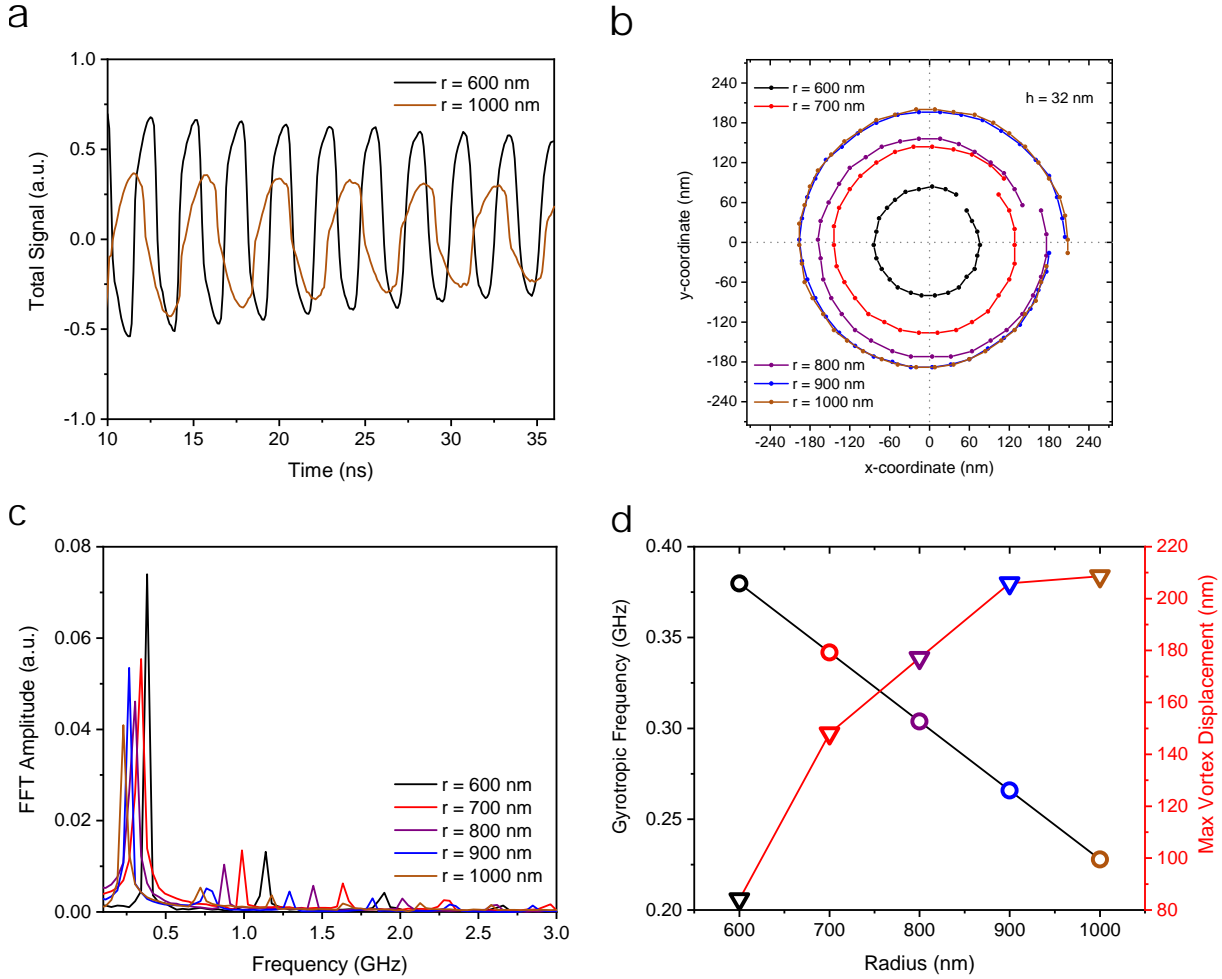
Figure 4.6: *(a) Time signal of the m_z oscillations of the right half of the disk for different radii (with a constant thickness of 32 nm) and their core trajectories (b) after a blockwave pulse of 200 ps for 5 mT field strength. (c) The frequency spectrum of the m_z oscillations shown in (a) and the gyrotropic frequency and maximum vortex displacement as a function of radius (d).*

The general trend is clear form Figure 4.6b, displaying the core trajectory for the different geometries. For larger radii, the vortex becomes more mobile until a radius of 900 nm is reached. Further increasing the radius has no significant effect on the vortex mobility. The gyrotropic frequency on the other hand decreases quite linearly when increasing the radius (black trace in Figure 4.6d).

An important distinction is worth to be emphasized here. As mentioned before, the behavior of the gyrotropic motion of the vortex core is studied here after applying a block wave pulse of 5 mT for 200 ps. The assumption is made here that when the disk is continuously excited at specifically the gyrotropic frequency, similar trends as observed in this section will still be valid.

4.2 CPW Simulation Results

The micromagnetic simulations indicate that 1-10 mT oscillating fields can induce the gyrotropic mode. These fields will be generated by CPWs and these must therefore be engineered and quantified carefully. The finite-element electromagnetic software tool Sonnet Pro was used to determine suitable designs for our CPWs. This software gives us the loss, impedance and current density profile as a function of frequency for the inserted structure. The following Figure 4.7 shows the CPW design (a), loss (S21) and impedance (b).
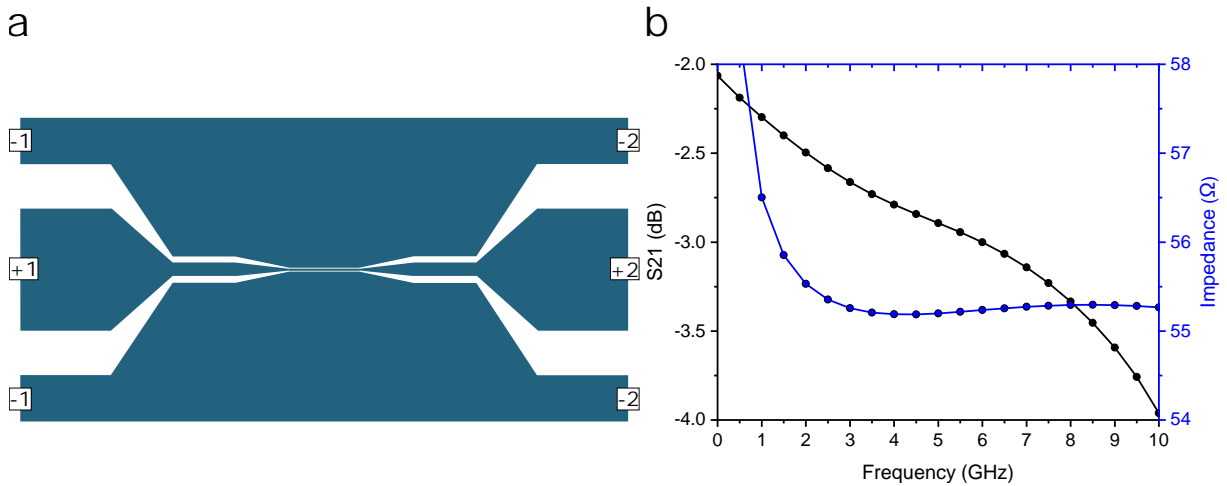
Figure 4.7: *Design showing the tempered stripline of the CPW (a) and loss S21/impedance (b) for this design.*

To abide the 50 Ohms impedance matching over a longer distance of the CPW, a tempered design was chosen with multiple trench and transmission line widths. The AC signal is applied between ports $+1$ and $+2$ and the -1 and -2 act as the connections to the ground planes. The location of these ports is where the electrical connections must be made. The following Figure 4.8 displays the current distribution (J_{xy}) of the complete waveguide for 1 GHz excitation (a) and at the middle of the waveguide, along a linecut in the y-direction for different frequencies at an applied power of 10 dBm (b). The loss of the waveguide is incorporated when calculating J_{xy} and the far majority of the current lies along the x-direction.
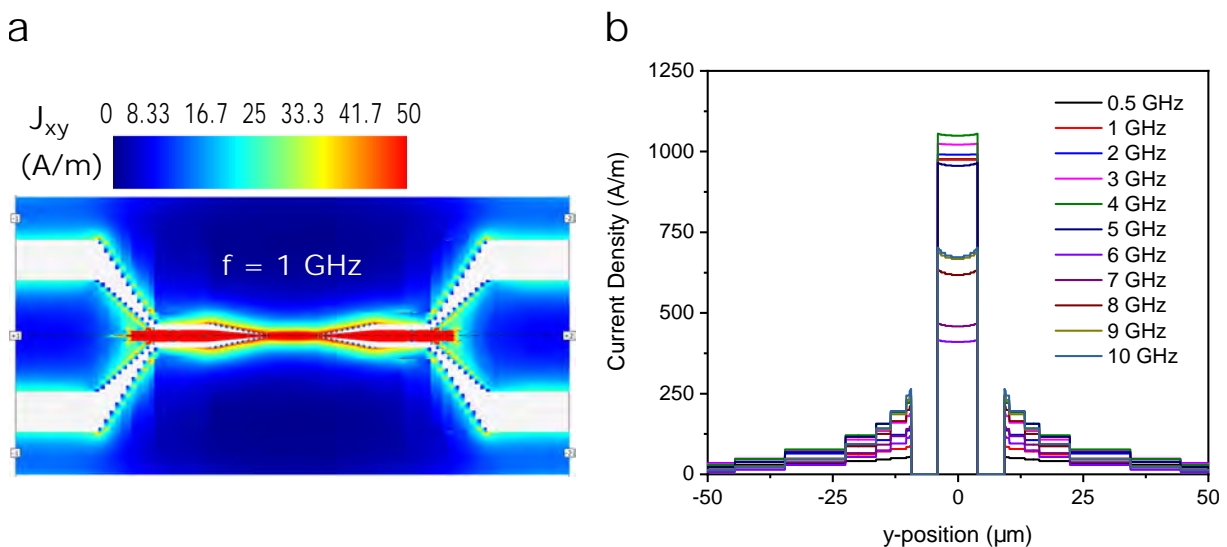
Figure 4.8: *Complete current density profile J_{xy} at an excitation frequency of 1 GHz (a) and linecuts in the middle of the transmission line for different frequencies at an excitation power of 10 dBm (b).*

The current density distribution is shown here in a small range ($0 - 50$ A/m) in order to emphasize the contrast between the smaller and larger structures.

As expected, as the transmission line becomes narrower, the current density of the AC signal becomes stronger. Current flow accumulation near the boundaries of the design as a result of the skin effect is also visible. The effect of applying higher power AC inputs to the waveguide can also be investigated with the software tool. Logically, stronger AC signals lead to higher current densities in the middle of the CPW and therefore stronger rotating Oersted fields. Figure 4.9a demonstrates this for three applied powers in terms of dBm at a frequency of 1 GHz. Figure 4.9b to the right sums up the Oersted field strengths generated for frequencies between $1 - 10$ GHz and three different power levels. A clear dip after 5 GHz is visible in all three traces and this dip becomes more significant for higher power levels. However, for even higher frequencies, all input power levels show a slight recovery in field strength. Our setup, using the power amplifier, can reach a maximum power level of 24 dBm. It becomes clear from this Figure that for the excitation of the gyrotropic mode ($f < 1$ GHz), this waveguide can generate fields up to 60 Oe. Although, one of course needs to take into account the loss of the lines leading to the CPW.
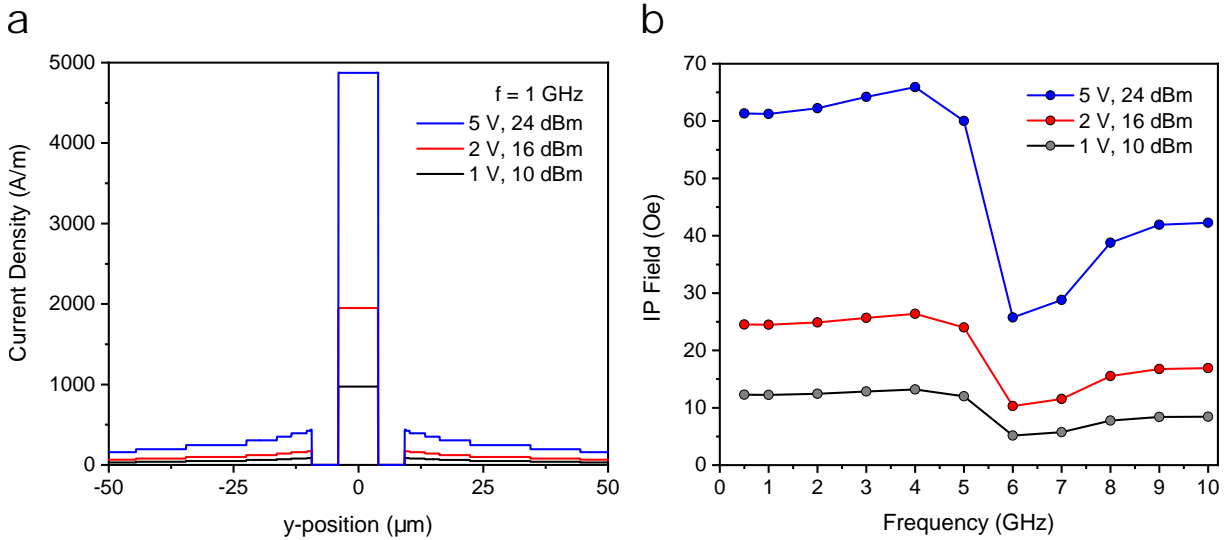
Figure 4.9: *(a) Current density along a linecut in the middle of the transmission line for different input powers at a frequency of 1 GHz. (b) The obtained IP Oersted field strengths as a function of frequency, shown for different applied powers.*

A comparison has also been made with regards to the previously utilized CPWs for which the generated field strengths are displayed with dashed lines in Figure 4.10a. The previous waveguides had geometric constants $s = 6.3$ μm and $w = 10$ μm. From Figure 4.10a, it becomes clear that the new CPWs (solid lines) can generate higher fields for lower frequencies, but lower ones for higher frequencies over 4 GHz. Since the focus of this thesis is on the excitation of the gyrotropic mode, the new CPW is more suited for this goal.

Of course the point can be made for decreasing the thickness of the waveguides to increase the current density and therefore the generated fields. However, sufficient impedance matching turns out to be difficult in thinner waveguides (as seen in Figure 4.10b). The geometric constants for the thickness ($h = 20$ nm) and trench s were modified, while the transmission line width was kept constant. The impedance was calculated for different s parameters but no significant improvement was visible. Even for lower frequency excitations, approximately 20 percent of the incident power remains. Furthermore, risk of cutting/damaging the CPW in the FIB step becomes more plausible when the waveguide is thinner.

a

b
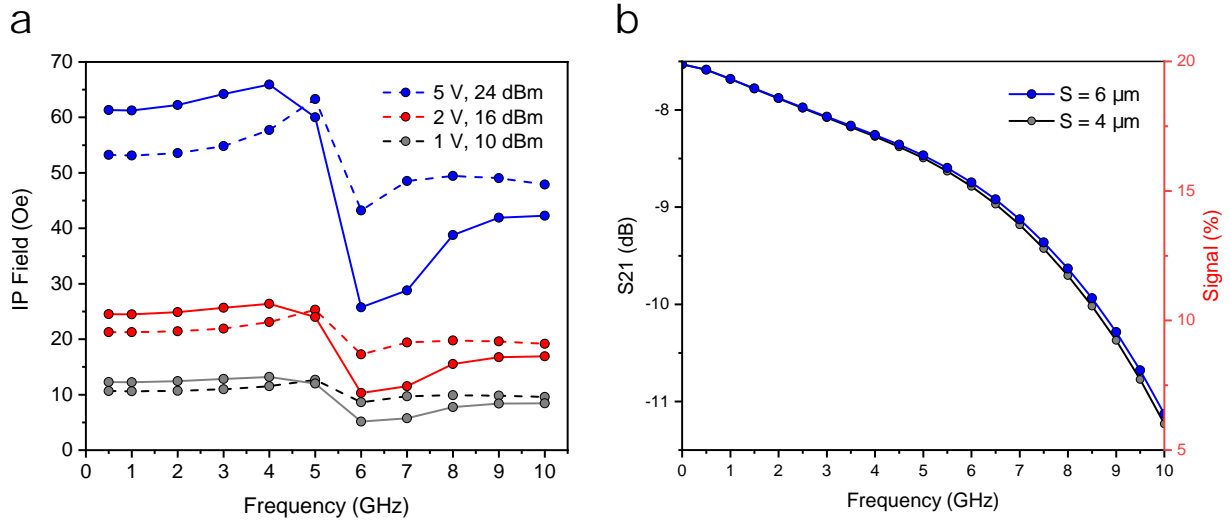
Figure 4.10: *(a) Comparison between the generated fields of the new (solid lines) and old (dashed lines) CPWs. The new CPW is clearly more suitable for the excitation of the gyrotropic mode. (b) The loss parameter S21 for the new CPW with a thickness of $h = 20$ nm.*

Another method with higher chances of succeeding is making the transmission line narrower, but this comes with its own complications (for instance alignment problems and the resist poisoning effect on Nb). Further geometric adjustments to improve the loss will be investigated, but one must be aware that the enlarged current densities in the CPW do not only result in stronger fields, but can plausibly heat the sample. In experiments, the effect on the critical current of local heating and spin texture alteration must be resolved.

4.3 Progress on the Experimental Setup

4.3.1 The new RF puck

Previously, a copper box was used to mount the substrate with CPW and Co disks to the high temperature insert of the vectormagnet (Figure 4.11a). This copper box was used to prevent the interference with back scattered RF signals. Furthermore, the dimensions of the box were chosen such to circumvent coupling with RF resonance modes of relevant frequencies. As can bee seen in Figure 4.11b, the loss was relatively decent, with less than -10 dB at a frequency of 1 GHz [28]. However, this substrate holder turned out to be quite troublesome with regards to making the electrical connections to the CPW and disks. Silver paint or epoxy were previously used to make all the connections, but especially for the contacts of the disks, this was inconvenient. Only 7×7 mm of space is available in the copper box and the sample contacts needed to be connected to conductive strips perpendicular to the plain of the sample.

a

b
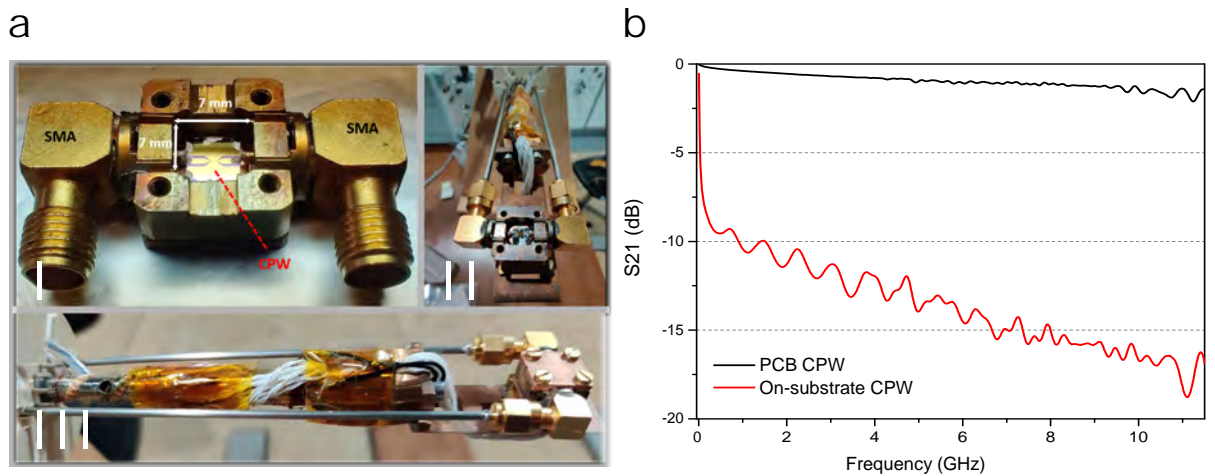
Figure 4.11: *(a) The old copper box used to mount the CPW. (b) The loss data of the CPW in the copper box (red trace) compared to a CPW on a printed circuit board (black trace).*

Figure 4.11b furthermore displays the excellent performance of a CPW on printed circuit board (PCB). This inspired the switch to a RF puck as seen in Figure 4.12a. The new puck can be simultaneously connected to the coax cables of the high temperature insert for RF excitation and to the electrical contacts for DC and AC measurements (inset II of 4.12a).

a

b
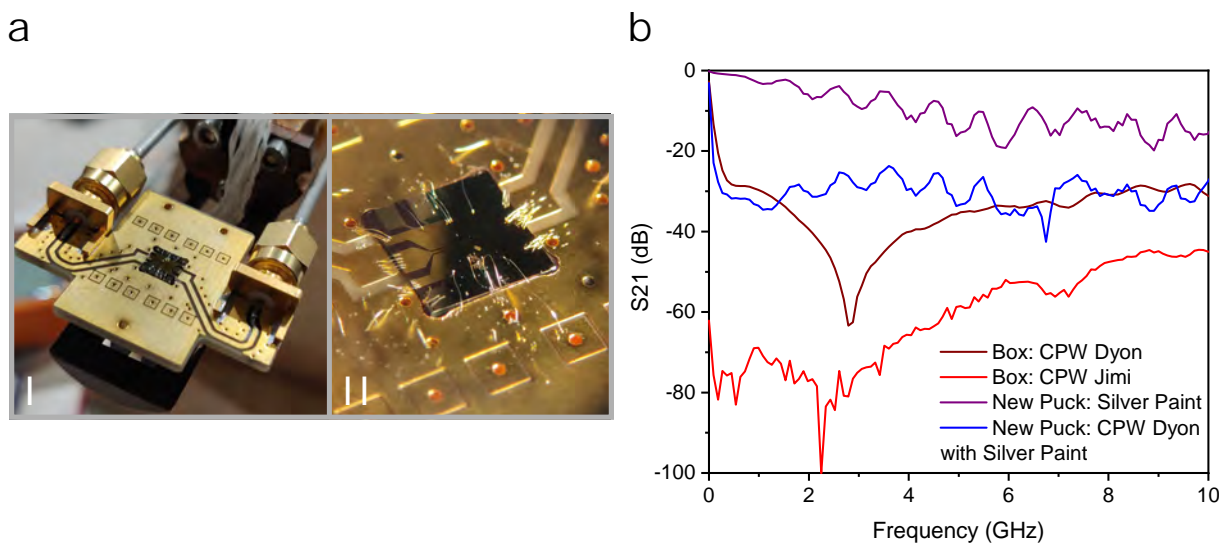
Figure 4.12: *(a) The new RF puck that can simultaneously be connected to the coax cables for RF excitation and the DC/AC contacts. (b) A close up of the sample with the wirebonds from the CPW on the puck to the CPW on the substrate.*

The connections to the signal/ground of the CPW and the ones to the Co/Nb disks can now all be made with wire bonds. Unfortunately, the first try relying completely on a multitude of wire bonds did not show the desired reduction in loss. Drastically more wire bonds to the AC pads of the CPW are expected to get a better impedance matching, making wire bonding the sample a time consuming endeavor. Therefore a combination of silver paint and wire bonds was chosen. Silver paint for the CPW and wire bonds for the disks results in the loss as displayed by the blue trace in Figure 4.12b. It is worth highlighting the experimental difficulties encountered in setting up RF-related measurements. For instance, the red trace in Figure 4.11b and the red trace in Figure 4.12b display two instances of the exact same experimental setup. However, two significantly different loss spectra were obtained. This was seen more than once and could have been caused by for example bad electrical connections with the silver paint/epoxy or the fragility of the SMA connectors.

To test the origin of the loss experienced by the setup, the loss of the wires to and in the insert were tested. These show consistent and acceptable behavior as visible in Figure 4.13a. Although the design of the CPW has been verified by the EM software results, different geometries were fabricated and measured. The width/gap of the transmission line/trench is kept constant in the different designs. Mainly the length of the part of the transmission line at its largest/smallest width was elongated (CPW 2/CPW 3). No significant different behavior was observed in these three designs (Figure 4.13b). This leads to the conclusion that the contact to the CPW on substrate is the most detrimental for the performance of the RF setup.
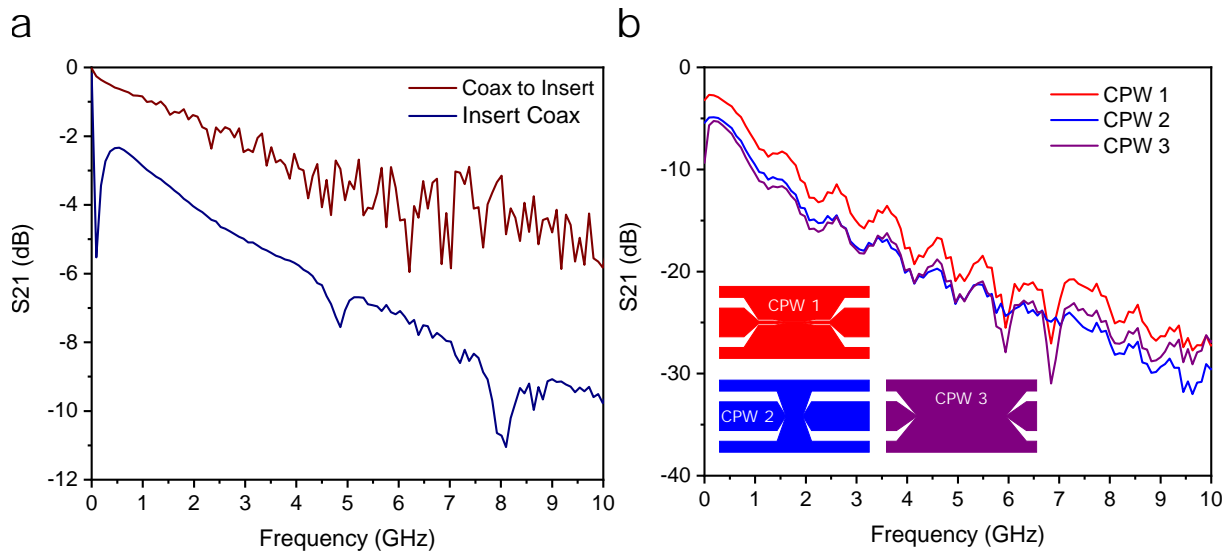

Figure 4.13: (a) The loss data of the coax cable to and inside the insert. (b) Inspection of the influence of different geometries on the loss of the CPW.

Taking the loss data of CPW 1 (which was generally used experimentally) to calculate the remaining power arriving at the middle of the transmission line after 24 dBm input at 1 GHZ excitation, one arrives at approximately 10 dBm. Here it is important to realize that the VNA measures the loss through the entire circuit. Therefore, the arriving power at the middle of the circuit is twice as big as initially calculated from the loss data. When relating this to the CPW simulation results, field strengths around 10 Oe can be achieved. This should be improved in order to get more significant FMR excitations in the disk. As mentioned before, this can be accomplished by geometric tuning of the sample and improving the contact to the CPW on the substrate. The following sections presents the experimental data acquired on static and dynamic disks.

4.4 Experimental Results

4.4.1 Static disks of larger radius

The first subject of the experimental results is a conventional Co/Nb disk with a radius of ~ 1.7 μm. The motivation for this experiment is two-fold: to compare its behavior to the conventional disks of ~ 1 μm and to test if they work successfully as spin triplet devices, since the larger disk will be more suited for memory applications. There will be more room for vortex movement and displacement of the hole further from the trench. All fabrication steps are as mentioned in the sample preparation section, with the exception of an adjusted FIB procedure to obtain the larger disk. A false colour scale SEM image of the sample is displayed in Figure 4.14a with to the right (Figure 4.14b) its resistance versus temperature graph. In contrast with superconducting films of one material, the R(T) of junctions show a clear two step transition. The first step signifies the larger parts of the structure (contacts and contact lines) entering the superconducting state. When the temperature is further reduced, the weak link of Cobalt (~ 30 nm) becomes increasingly more proximized and the resistance finally reaches zero. A clear and wide two step transition is also an indication for the absence of a significant residual Nb layer between the two halfs of the disk. This is opposed to a singlet junction that would have a narrow secondary step.

a

b

c

d
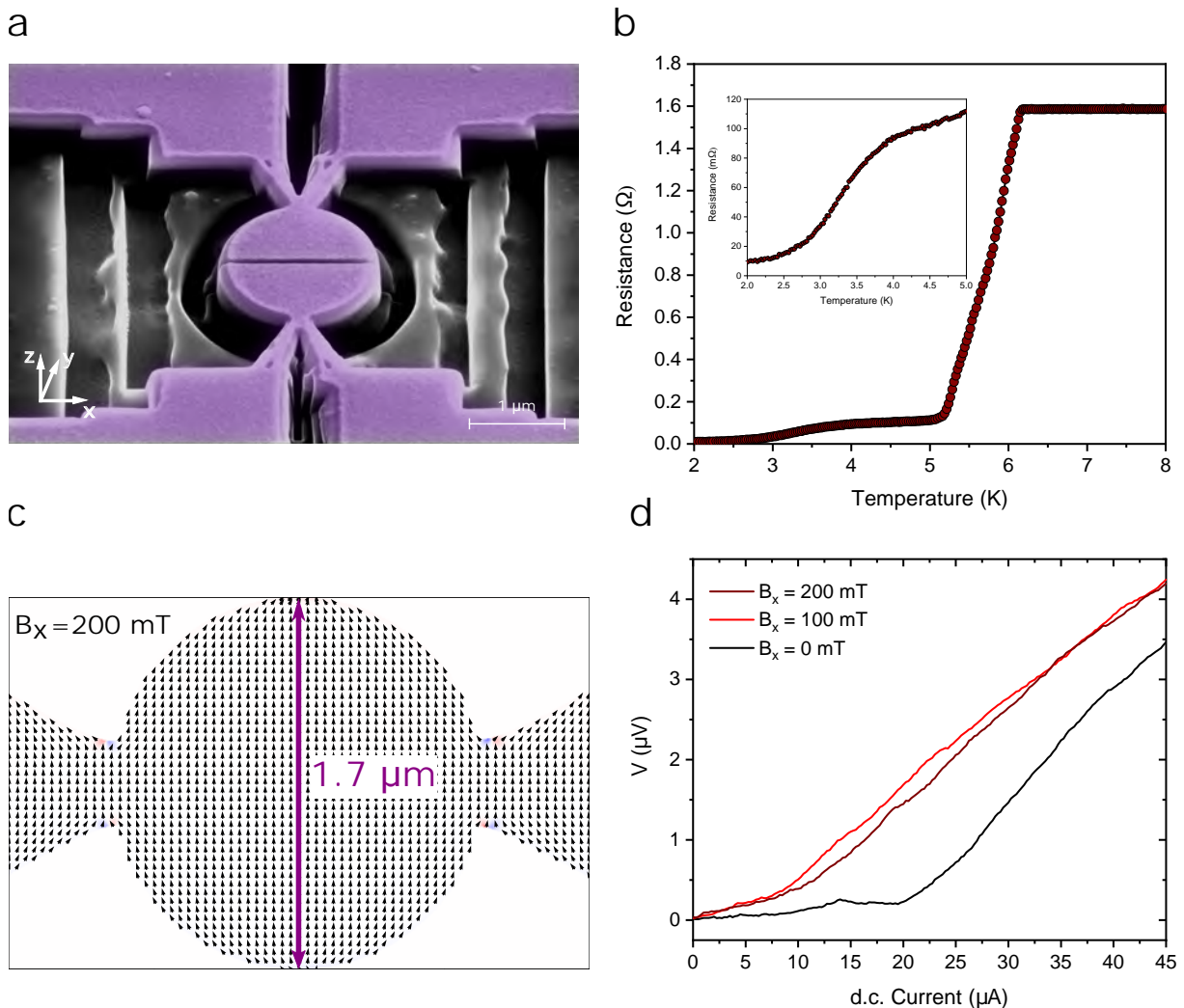
Figure 4.14: *(a). False colour scaled SEM image of the conventional Co/Nb disk with a diameter of ~ 1.7 μm. (b) Resistance versus temperature graph, R(T), measured under a current bias of 10 μA. The R(T) shows a clear two step transition, indicative of Josephson junctions. The inset represents the second transition displayed in a lower resistance range. (c) When an IP field of 200 mT is applied along the trench in the disk, the spin texture of the vortex vanishes, leaving a magnetic configuration almost completely magnetized along the x-direction. (d) Since no spin texture gradient is present at high IP fields, a suppressed critical current is observed.*

If a significant Nb layer would be present, a large background singlet contribution ($\sim$ 50-100 μA) would be observed in the experimental data. The initial test performed to check for the presence of a triplet junction is done by applying strong magnetic IP fields, demagnetizing the disk in one direction. This will get rid of all the spin-texture and therefore all the triplet generation. Any observed supercurrent at these IP fields should be considered as the singlet background.

As seen in previous experiments of disks with a diameter of $\sim$ 1 μm, a clear SQUID oscillation is visible (Figure 4.15a and b) for larger disks as well, indicating the splitting of the supercurrent in two separate arms. The period of the SQUID oscillation is $\sim$ 3 mT, consistent with the enclosed flux.

a

b

c
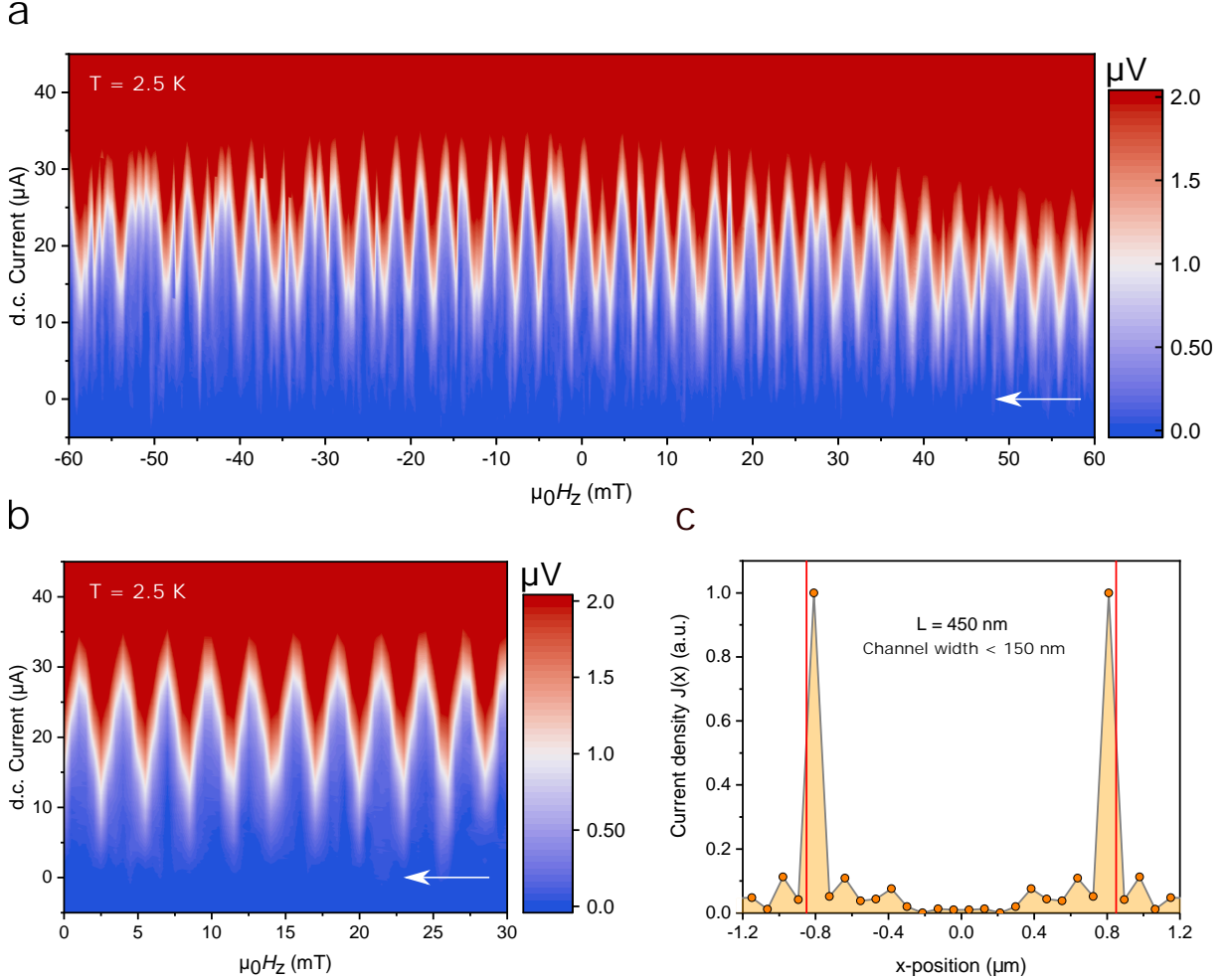
Figure 4.15: (a) Interference pattern at 2.5 K showing a large number of SQUID oscillations measured while sweeping the field in the OOP direction from +60 mT to −60 mT. Glitches in the SQUID oscillations are caused by superconducting vortices entering and leaving the system. (b) Clean SQUID interference pattern used for the Fourier procedure to calculate the spatial current density J(x) seen in (c).

The supercurrent spatial density profile $J(x)$ can more accurately be determined from the interference pattern $I_c(H)$ due to the Fourier transform relation between the two, as described by Dynes and Fulton [29], according to:

$$J(x) \sim \int_{-\infty}^{+\infty} dB I_c(B) \exp \frac{2\pi i LBx}{\phi_0} \qquad (4.1)$$

Here, the magnetic field B lies along the z-axis, the critical current I_c along the y-axis and the supercurrent density distribution $J(x)$ is resolved along the x-axis. Furthermore, $\phi_0 = h/2e$ is the flux quantum and L is the effective length of the junction. The contour of the SQUID pattern of Figure 4.15b is used for the Fourier procedure (with $L = 450$ nm) and results in the spatial supercurrent density $J(x)$ as plotted in 4.15c. The same behavior previously observed in conventional disks of $\sim$ 1 μm diameter

is apparent here as well. The supercurrent splits in two arms, tightly confined to the edges of the sample. Practically no spincurrent is present in the middle of the disk close to the magnetic vortex core. This supercurrent profile fortifies the argument that the boundary between spin texture gradient, superconductor and vacuum plays an essential role in the triplet generation as theorized by Silaev et al. (theoretical work in progress).
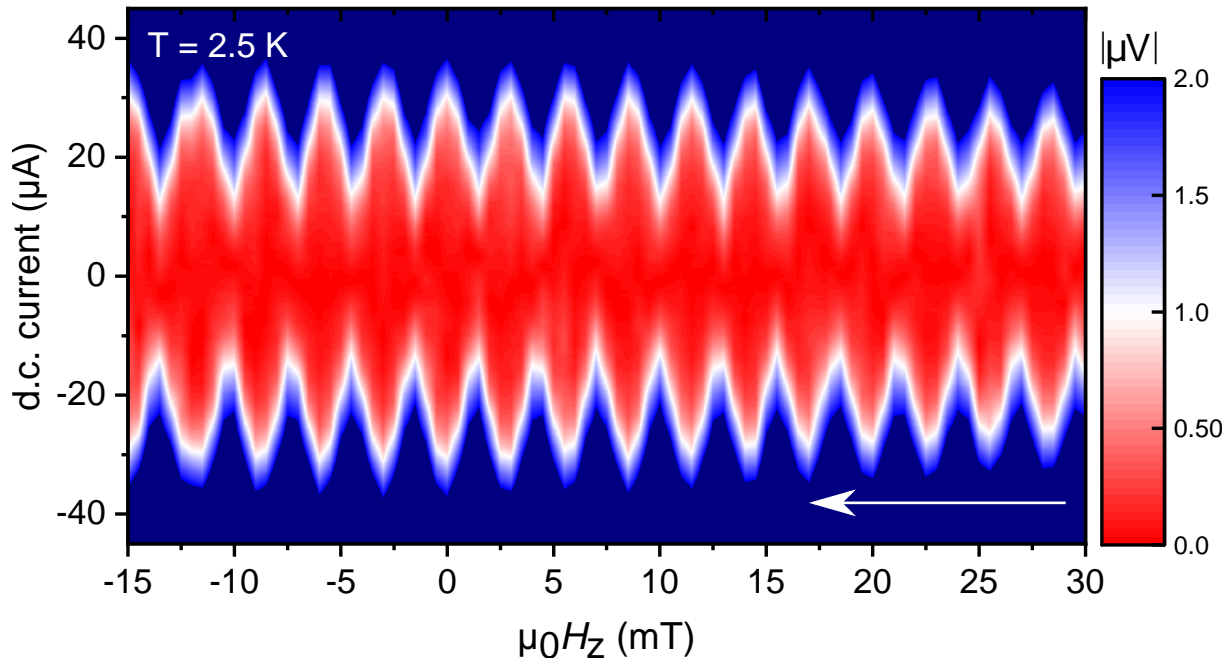
Figure 4.16: *Symmetric interference pattern for both positive and negative current bias, testifying the clean SQUID behavior of the junction.*

As a final test, the symmetry of the SQUID pattern was investigated by measuring both the developed voltage for both negative and positive currents. The result is presented in Figure 4.16 for a back sweep starting at 30 mT and ending at −15 mT. Here the developed voltage is displayed in absolute values. Clearly apparent from this Figure is the symmetry of the interference pattern. This section demonstrated the successful operation of a disk structure with a radius of ~ 1.7 μm as a spin triplet device. Therefore it was shown that (within limits) we can change the radius of the disk without fundamentally altering the behavior of the spin triplet supercurrent. The most important and consistent feature presented here is the splitting of the supercurrent into two paths, tightly confined to the edge of the sample.

The following section takes a closer look at utilizing these disks as superconducting memory applications by introducing a hole displaced perpendicular to the trench.

4.4.2   Static disks with hole geometries

The second subject of the experimental results is a conventional Co/Nb disk with a diameter of $\sim 1~\mu$m with a hole of diameter ~ 100 nm, with its center located ~ 120 nm from the trench. All fabrication steps are again as mentioned in the sample preparation section, with the exception of an additional FIB step to obtain the hole. A false colour scale SEM image of the sample is displayed in Figure 4.17a with to the right (Figure 4.17b) its respective resistance versus temperature graph. No clear two step transition is observed, indicating the presence of a residual layer of Nb in the trench and a large singlet background.

a

b
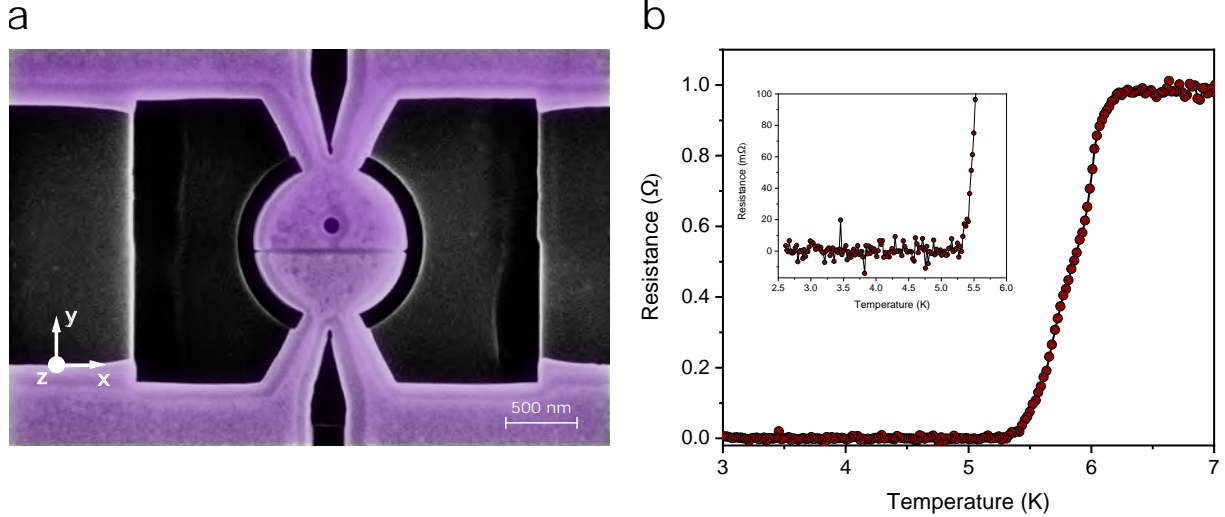
Figure 4.17: *(a). False colour scaled SEM image of the Co/Nb disk with a diameter of $\sim 1~\mu$m and a hole with a diameter of ~ 100 nm with its origin at a distance of ~ 120 nm from the trench. (b) Resistance versus temperature graph, $R(T)$, measured under a current bias of $10~\mu A$ of the disk with hole geometry. The $R(T)$ does not show a clear two step transition, indicative of large singlet background and a residual layer of Nb.*

The goal of this experiment is to demonstrate superconducting memory signified by an alteration in the critical current. The initial idea was to push the magnetic vortex in/out of the hole with IP fields, leading to two stable ground state at zero applied field as discussed ins section 4.1.2. The two states will have differing spin textures and therefore a reduced/increased critical current. Figure 4.18 shows the dV/dI of four different subsequent field sweeps in the x-direction, moving the vortex perpendicular to the trench in the y-direction. A clear and abrupt increase in the critical current is observed in all four sweeps, with the location of the increase mirrored when the sweep direction is reversed. The increase is hypothesized to be caused by the vortex deforming when it gets closer to the hole. This deformation leads to a drastic boost of the spin gradient close to the trench, resulting in a higher supercurrent. But the exact origin of this sudden increase in I_c is still debated.
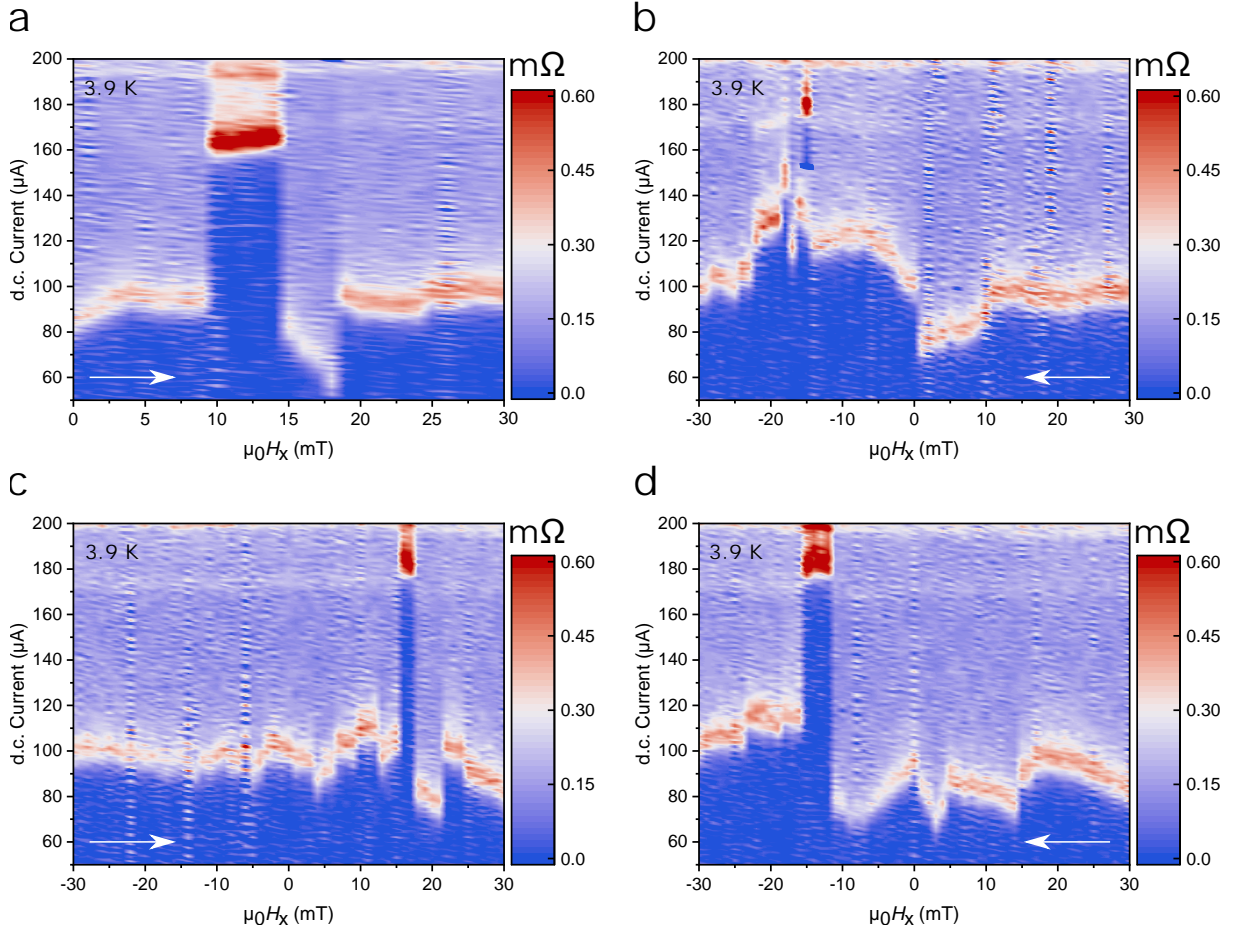
Figure 4.18: (a) Measurement of the I_c at 3.9 K while sweeping the field IP along the x-direction from 0 mT to +30 mT. (b) The sweep direction is reversed, measuring the I_c while sweeping from +30 mT to −30 mT. In both sweep directions, a clear increase in I_c is observed, hypothesized to correspond to the movement of the vortex core. (c-d) The experiment was repeated and the current peak was reproducible in height and location.

The location of the increase in critical current is reproducible and can therefore be used to systematically switch between a high and low supercurrent state at zero applied field. The temperature was raised to 4.7 K to enhance the current ratio between the two states. When the field is swept along the x-direction until 16 mT (corresponding to the location of the supercurrent peak) and then swept back to zero field, a clear difference between the zero field currents can be observed (Figure 4.19a and b).
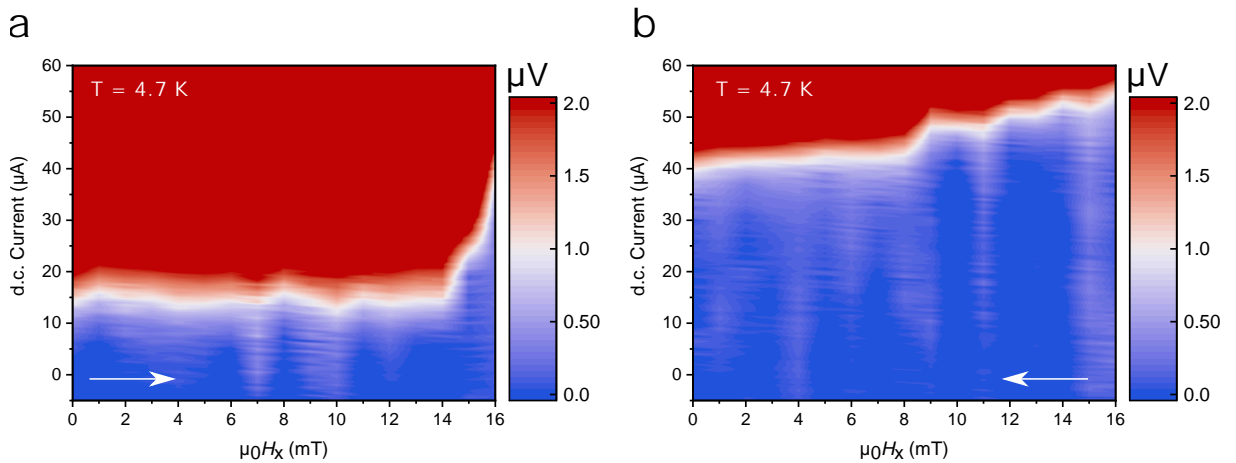

Figure 4.19: (a) Switching between the two current states of the device with the zero field data corresponding to the low current state. (b) When sweeping back to zero IP field after reaching the current peak, an enhanced critical current state is maintained.

A recent report [30] presented a 60 percent change in critical current in the two magnetic configurations of their multilayered sample. Here we measure a low current state of ~ 11 μA and a high current state of ~ 36 μA, an increase of 227 percent. Unfortunately, when resetting the magnetic configuration of the device by applying a strong OOP field of 1 T followed by relaxation, the memory behavior could not be reproduced. The reason for this is unknown, but could have been caused potentially by a superconducting vortex initially being trapped by the magnetic vortex core and influencing the transport characteristics.

4.4.3 Dynamic disks on CPWs

The final subject of the experimental results are the Co/Nb disks with diameter $\sim 1~\mu m$ on the CPW. The fabrication steps are as described in the preparation section with the inclusion of the modified FIB steps as presented in section 3.1.3. The first measured structure on a CPW could unfortunately not be connected to the RF-input due to the complications with the copper box as mentioned in section 4.3. Nonetheless, the operation of the disk on the CPW is measured and compared to the conventional disks directly on the substrate. A false colored SEM image of such a disk on CPW is displayed in Figure 4.20a with to the right its R(T) (Figure 4.20b). Again a two-step transition is measured.
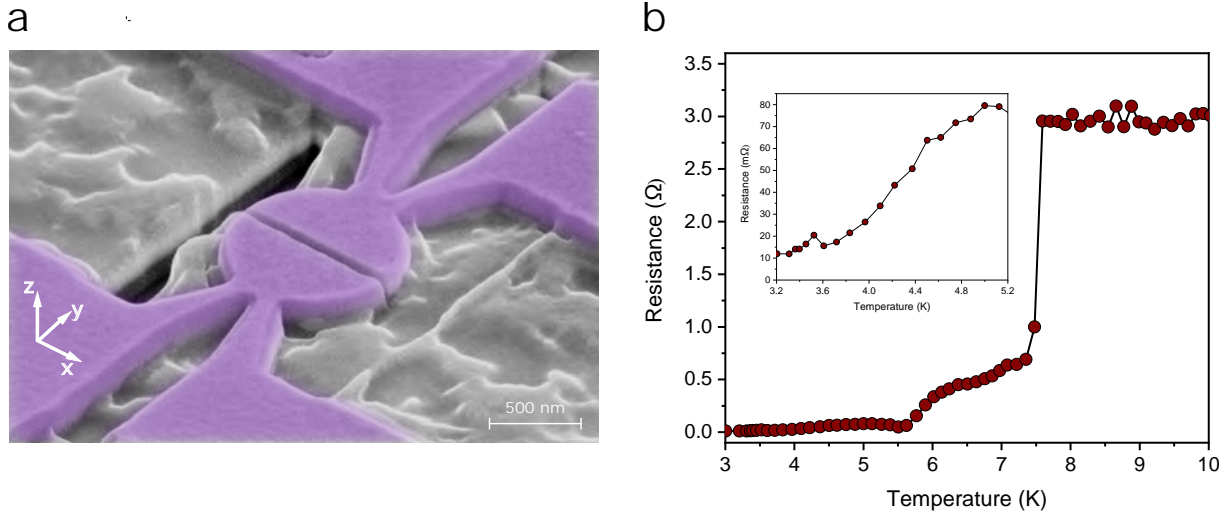
Figure 4.20: (a). False colour scaled SEM image of the Co/Nb disk with a diameter of $\sim 1~\mu m$ on the CPW. Slight damage to the CPW is visible next to the disk to the left, caused by the non-uniform milling during the FIB process. (b) $R(T)$ measured under a current bias of 10 μA.

When measuring the SQI pattern at 1.5 K, while sweeping the field in the OOP direction from 20 mT to -20 mT, a clear SQUID pattern was once more visible (Figure 4.21a). The period of the oscillation is approximately 7 mT, in accordance with previously measured devices. To check for the presence of a singlet background current, the field was swept in the IP field direction along the x-direction from 200 mT to -200 mT (Figure 4.21b).
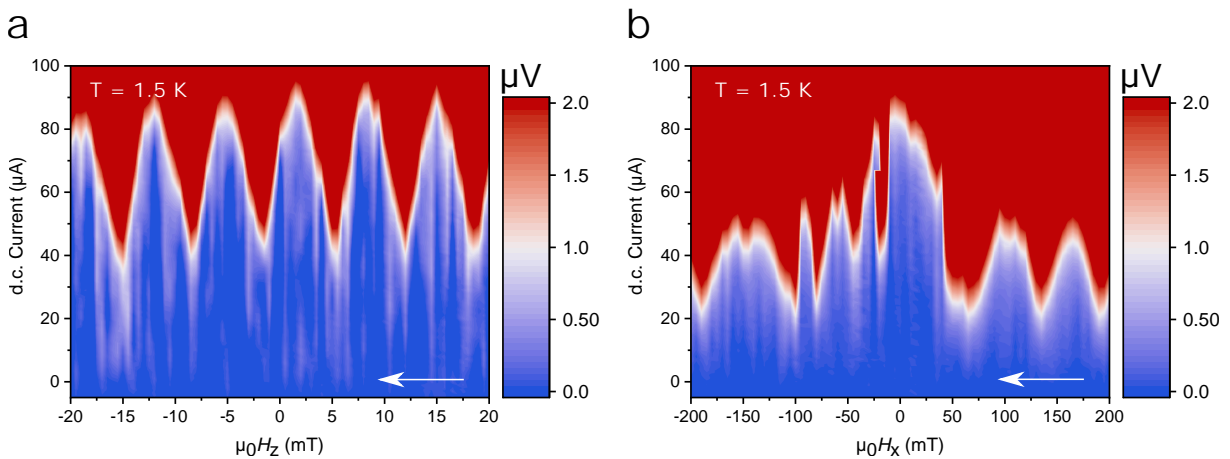
Figure 4.21: (a) SQUID oscillation of the disk on CPW measured at 1.5 K when sweeping the field in the OOP direction from 20 to -20 mT. (b) Measurement of the critical current while sweeping the field IP along the x-direction from 200 mT to -200 mT. Features of a singlet interference pattern are visible, expected to come from the smaller junction area in the zy-plane. Noticeably, the background in the oscillation measured in (a) corresponds to the current of $\sim 20\mu A$ at $B_x = 200$ mT in Figure 4.21 (b).

At $H_x = 200$ mT, the entire sample is demagnetized in the x-direction, leaving no spin texture present and therefore no triplet current. The supercurrent present here are singlet correlations. Noteworthy, the I_c observed at 200 mT IP field corresponds with the background observed in the oscillation in Figure 4.20a.

As mentioned before, the RF excitation can induce heating in the disk. This could lead to a rise in sample temperature and therefore a reduction of the critical current. The effect of heating on the current through the junction must therefore be resolved from the effect of the RF excitation. Figure 4.22a displays how the sample temperature changes while a frequency sweep is performed at an input power of 16 dBm. The temperature rises between $3 - 4$ GHz and $5 - 6$ GHz. These frequencies are expected to be resonance modes in the sample chamber.

a

b
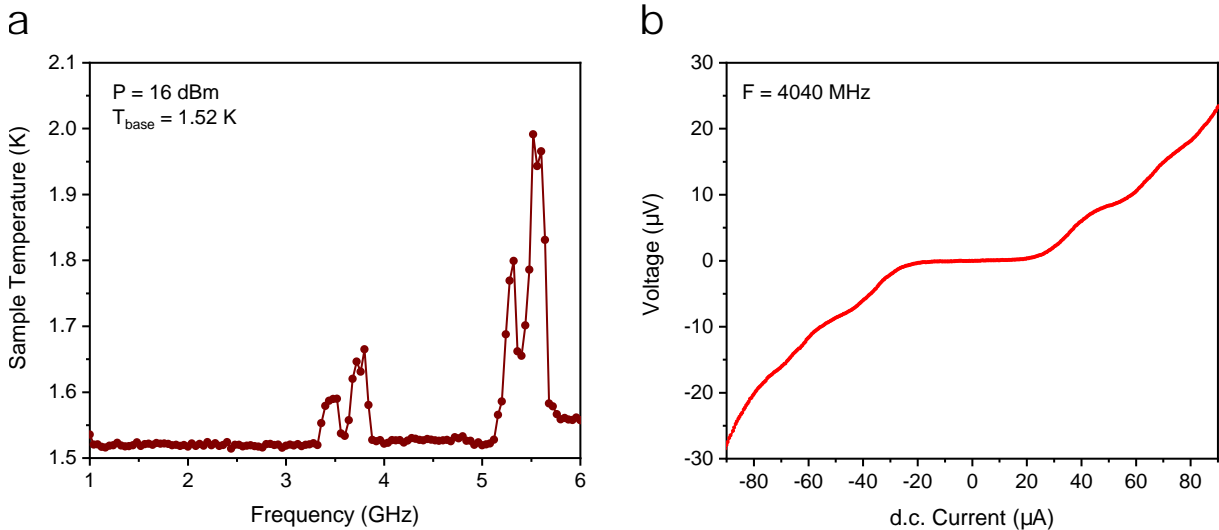
Figure 4.22: *(a) The effect of RF excitation of the CPW on the sample temperature at an input level of 16 dBm. Four distinct peaks are visible, expected to relate to resonance modes in the sample chamber. (b) Shapiro steps at a frequency excitation of 4040 MHz. The measured Shaprio steps occur at irregular frequencies and are hypothesized to be caused by backscattered RF signals.*

Furthermore, the effect of the CPW excitation on the critical current is already visible in the form of Shapiro steps in the IV characteristics. Figure 4.22b presents this for a frequency excitation of 4040 MHz. However, the Shapiro steps occur at irregular frequencies and are therefore hypothesized to come from backscattered RF signals. A copper cap was made to shield the sample from these signals.

CHAPTER
Conclusions and Outlook

Firstly, significant progress has been made on the RF set-up, enabling simultaneous high frequency excitation and four-probe measurements on samples on waveguides. However, the loss experienced by the CPW needs to be significantly improved to reach sufficient field strengths. Most of this loss is thought to be caused by the connection to the substrate. This could potentially be solved by exploring a whole new avenue to reduce the loss experienced by the CPWs. Commonly used in FMR experiments are air coplanar probes (Figure 5.1a), which are specifically designed for impedance matched contact with the substrate and therefore low loss in a broadband spectrum. These probes are available for cryogenic environments and in ground-signal-ground geometries (Figure 5.1b).

a

b
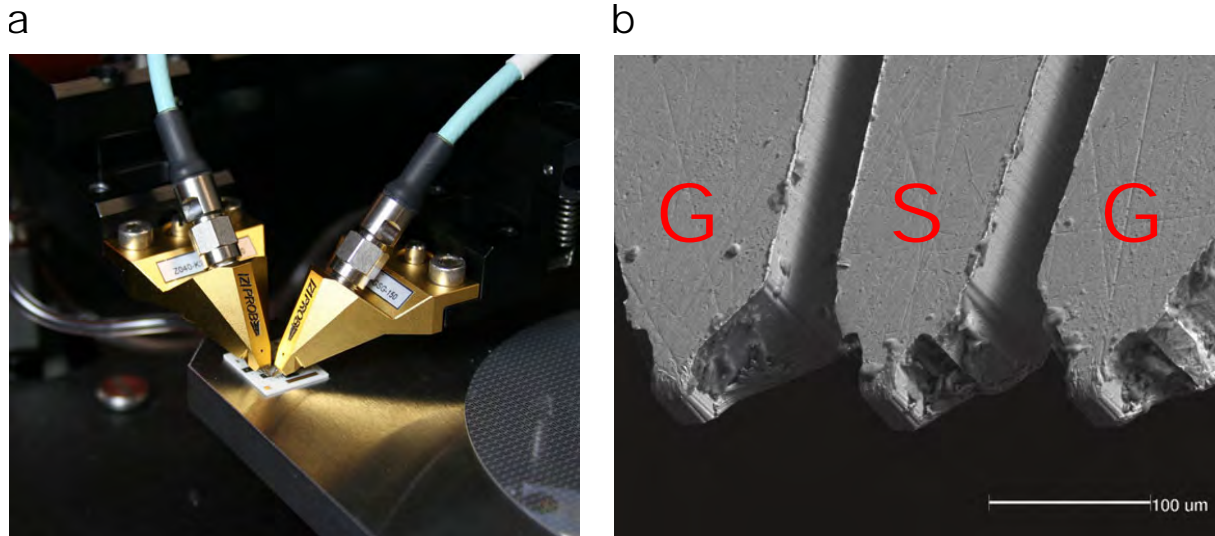
Figure 5.1: *(a) Example of the landed Z Coaxial air probes from FormFactor, Inc. (b) SEM image displaying the ground (G) and signal (S) contacts of the probes.*

The challenge would be to incorporate these probes in a modified RF puck. Usually the contact is made using mechanical micromanipulators, but a setup using a spring would suffice as well as long as the probes can be fixed in place.

Secondly, clear SQUID behavior in static Co/Nb disks of different radii has been observed. This fortifies the notion of the splitting supercurrent, confined closely to the boundaries of the disk. This in turn makes a favorable argument for the theory on spin triplet generation of Sileav (theoretical work in progress) in which the boundary between superconductor, ferromagnet with spin texture gradient and vacuum plays a central role. Furthermore, although not conclusive, the superconducting memory of disks with hole geometries shows promises. A significant difference between the low and high critical current state caused by the two magnetic ground states is measured. Lastly, the disk on the CPW perform as expected manifesting again a SQUID interference pattern. The first disks on CPW that could be measured while RF excitation takes place have a large singlet component. However, the effect of the RF excitation through the CPW was already observed in the form of Shapiro steps. These are hypothesized to be caused by backscattered RF signals.

Acknowledgements

I would first and foremost like to thank my main supervisors, Professor Jan Aarts and Dr. Kaveh Lahabi. Professor Aarts has always been supportive and at all times his door was open to discuss the developments and plans during my project. Dr. Lahabi has taught me more about the field of Josephson junctions than I thought possible during my master project. Both of them engaged in discussions with an open mind and I truly felt they appreciated my input. Therefore, it comes as no surprise that I enjoyed the collaboration thoroughly. Furthermore, I would like to thank PhD candidates Remko Fermin and Guerino Avallone for their collaboration and positive attitudes. They have fortified my belief that the academic community can be a wonderful place to work. The technical support of Douwe Scholma, Thomas Mechielsen and Marcel Hesselberth is appreciated immensely and therefore I would like to thank them as well for their quick and effective aid. Lastly, I would like to express the gratitude I feel towards my family and friends, one could not hope to find a more supportive environment than the one I have had the luck to enjoy.

References

[1] K. Lahabi, *Spin-triplet supercurrents of odd and even parity in nanostructured devices*, PhD Dissertation, Leiden University (2018).

[2] M. Hubert, *Using Josephson junctions as superconducting memory devices*, MSc Thesis, Leiden University (2018).

[3] F. Bergeret, A. Volkov, and K. Efetov, *Long-range proximity effects in superconductor-ferromagnet structures*, Phys. Rev. Lett. **86(18)**, 4096 (2001).

[4] M. Houzet and A. I. Buzdin, *Long range triplet Josephson effect through a ferromagnetic trilayer*, Phys. Rev. B **76(6)**, 060504 (2007).

[5] N. Banerjee, J. W. A. Robinson, and M. G. Blamire, *Reversible control of spin-polarized supercurrents in ferromagnetic Josephson junctions*, Nature Communications **5**, 1 (2014).

[6] M. A. Khasawneh, T. S. Khaire, C. Klose, W. P. Pratt Jr, and N. O. Birge, *Spintriplet supercurrent in Co-based Josephson junctions*, Superconductor Science and Technology **24(2)**, 024005 (2011).

[7] B. D. Josephson, *Possible new effects in superconductive tunnelling*, Physics Letters **1(7)**, 251 (1962).

[8] M. Mosley, *Presentation: Magnetism on the Move*, US-Spain Workshop on Nanomaterials , 10.

[9] R. Antos, Y. C. Otani, and J. Shibata, *Magnetic Vortex Dynamics*, J. Phys. Soc. Jpn. **77**, 031004 (2008).

[10] . J. Shibata, Y. Nakatani, G. Tatara, H. Kohno, and Y. Otani, *Magnetic vortex dynamics induced by spin-transfer torque*, Journal of Magnetism and Magnetic Materials **310**, 2041 (2007).

[11] G. M. Wysin and W. Figueiredo, *Thermal vortex dynamics in thin circular ferromagnetic nanodisks*, Phys. Rev. B **86**, 104421 (2012).

[12] V. Sluka, T. Schneider, R. A. Gallardo, A. Kákay, M. Weigand, T. Warnatz, R. Mattheis, A. Roldán-Molina, P. Landeros, V. Tiberkevich, A. Slavin, G. Schütz, A. Erbe, A. Deac, J. Lindner, R. J., J. Fassbender, and S. Wintz, *Emission and propagation of 1D and 2D spin waves with nanoscale wavelengths in anisotropic spin textures*, Nature Nanotechnology **14**, 328 (2019).

[13] I. Neudecker, K. Perzlmaier, F. Hoffmann, G. Woltersdorf, M. Buess, D. Weiss, and C. H. Back, *Modal spectrum of permalloy disks excited by in-plane magnetic fields*, Phys. Rev. B. **73**, 134426 (2006).

[14] M. Bolte, G. Meier, B. Krüger, A. Drews, R. Eiselt, L. Bocklage, S. Bohlens, T. Tyliszczak, A. Vansteenkiste, B. Van Waeyenberge, K. W. Chou, A. Puzic, and H. Stoll, *Time-Resolved X-Ray Microscopy of Spin-Torque-Induced Magnetic Vortex Gyration*, Phys. Rev. Lett. **100**, 176601 (2008).

[15] J. P. Park, P. Eames, D. M. Engebretson, J. Berezovsky, and P. A. Crowell, *Imaging of spin dynamics in closure domain and vortex structures*, Phys. Rev. B. **67**, 020403 (2003).

[16] S.-B. Choe, Y. Acremann, A. Scholl, A. Bauer, A. Doran, J. Stöhr, and H. Padmore, *Vortex Core-Driven Magnetization Dynamics*, Science **304**, 420 (2004).

[17] B. Van Waeyenberge, A. Puzic, H. Stoll, K. W. Chou, T. Tyliszczak, R. Hertel, M. Fähnle, H. Brückl, K. Rott, G. Reiss, I. Neudecker, D. Weiss, C. H. Back, and G. Schütz, *Magnetic vortex core reversal by excitation with short bursts of an alternating field*, Nature Letters **444**, 461 (2006).

[18] V. Novosad, F. Y. Fradin, P. E. Roy, K. S. Buchanan, K. Y. Guslienko, and S. D. Bader, *Magnetic vortex resonance in patterned ferromagnetic dots*, Phys. Rev. B. **72**, 024455 (2005).

[19] J. P. Park and P. A. Crowell, *Interactions of Spin Waves with a Magnetic Vortex*, Phys. Rev. Lett. **95**, 167201 (2005).

[20] M. Kammerer, M. Weigand, M. Curcic, M. Noske, M. Sproll, A. Vansteenkiste, B. Van Waeyenberge, H. Stoll, G. Woltersdorf, C. H. Back, and G. Schütz, *Magnetic vortex core reversal by excitation of spin waves*, Nature Communications **2**, 1 (2011).

[21] M. Buess, R. Höllinger, T. Haug, K. Perzlmaier, U. Krey, D. Pescia, M. R. Scheinfein, D. Weiss, and C. H. Back, *Fourier Transform Imaging of Spin Vortex Eigenmodes*, Phys. Rev. Lett **93**, 077207 (2004).

[22] A. Vansteenkiste, J. Leliaert, M. Dvornik, M. Helsen, F. Garcia-Sanchez, and B. Van Waeyenberge, *The design and verification of MuMax3*, AIP advances **4**, 107133 (2014).

[23] http://wcalc.sourceforge.net/cgi bin/coplanar.cgi.

[24] O. Karlqvist, *Calculation of the magnetic field in ferromagnetic layer of a magnetic drum*, Transactions of the Royal Institute of Technology Stockholm, Sweden , 13 (1954).

[25] I. Neudecker, *Magnetization Dynamics of Confined Ferromagnetic Systems*, PhD Dissertation, University of Regensburg (2006).

[26] E. R. P. Novais and A. P. A.P. Guimaraes, *Phase diagram of magnetic configurations for soft magnetic nanodots of circular and elliptical shape obtained by micromagnetic simulation*, arXiv:0909.5686 (2009).

[27] J. Aretz, *The Cobalt Disk as a Superconducting Memory Element*, BSc Thesis, Leiden University (2020).

[28] J. D. de Haan, *Towards Spin Triplet Superconducting junctions in a Dynamic Regime*, MSc Thesis, Leiden University (2020).

[29] R. C. Dynes and T. A. Fulton, *Supercurrent Density Distribution in Josephson Junctions*, Phys. Rev. B **3**, 3015 (1971).

[30] N. Satchell, P. M. Shepley, M. Algarni, M. Vaughan, E. Darwin, M. Ali, M. C. Rosamond, L. Chen, E. H. Linfield, B. J. Hickey, and G. Burnell, *Spin-valve Josephson junctions with perpendicular magnetic anisotropy for cryogenic memory*, Appl. Phys. Lett. **116**, 022601 (2020).